Bauhaus-Universität Weimar

Doctoral Thesis

Goal-Oriented Adaptive Modeling of 3d Elastoplasticity Problems

Author:
Seyed Shahram Ghorashi

Supervisor:
Prof. Dr.-Ing. Timon Rabczuk

A thesis submitted in fulfillment of the requirements
for the degree of Doctor of Philosophy

in the

Research Training Group 1462
Faculty of Civil Engineering

September 2016

Ehrenwörtliche Erklärung

Ich erkläre hiermit ehrenwörtlich, dass ich die vorliegende Arbeit ohne unzulässige Hilfe Dritter und ohne Benutzung anderer als der angegebenen Hilfsmittel angefertigt habe. Die aus anderen Quellen direkt oder indirekt übernommenen Daten und Konzepte sind unter Angaben der Quellen gekennzeichnet. Weitere Personen waren an der inhaltlich-materiellen Erstellung der vorliegenden Arbeit nicht beteiligt. Insbesondere habe ich hierfür nicht die entgeltliche Hilfe von Vermittlungs-bzw. Beratungsdiensten (Promotionsberater oder anderer Personen) in Anspruch genommen. Niemand hat von mir unmittelbar oder mittelbar geldwerte Leistungen für Arbeiten erhalten, die im Zusammenhang mit dem Inhalt der vorgelegten Dissertation stehen. Die Arbeit wurde bisher weder im In-noch im Ausland in gleicher oder ähnlicher Form einer anderen Prüfungsbehörde vorgelegt. Ich versichere ehrenwörtlich, dass ich nach bestem Wissen die reine Wahrheit gesagt und nichts verschwiegen habe.

Seyed Shahram Ghorashi
Weimar, July 2016

Abstract

Development of an efficient adaptivity methodology for analysis of three-dimensional elastoplasticity problem in order to achieve an accurate solution of a quantity of interest is highly demanded. 3D simulation of elastoplastic material is an important engineering tool which plays a significant role in the analysis and design of numerous engineering applications, e.g. prediction of ductile failure. Since it is a nonlinear problem, its computational cost is notably increased by uniformly refining the mesh when very accurate result is required. Accordingly, mesh adaptation based on a reliable error estimation method would be a profitable tool.

The conventional error estimation approaches estimate the energy error norms while accuracy of some quantities, such as point displacement or average stresses in a specific domain are of most interest. Goal-oriented error estimation methodology has been developed based on this fact to be able to estimate the solution error according to the quantity of interest.

For this purpose, the dual-weighted residual error estimation, which is a robust goal-oriented error estimation, is used. It is a dual-based scheme which requires an adjoint problem defined according to the quantity of interest. Afterwards, estimated element-wise errors are exploited for performing goal-oriented mesh adaptivity procedure. By applying tetrahedron and hexahedron elements for the FEM analysis in 2D and 3D cases, respectively, hanging nodes are introduced in the refinement process. They are constrained in order to preserve their compatibility with the adjacent nodes.

In this contribution, the elastoplasticity analysis is performed in both cases of load and displacement based control. Error in quantity of interest is computed at each load/displacement increment and mesh adaptation based on coarsening and refinement is considered when the error norm reaches a specified value. The nodal solutions and history variables at Gauss points are transferred and projected to the new mesh after each mesh adaptation.

This goal-oriented mesh adaptivity method is applied in several 2D/3D, elastic/elasto-plastic numerical examples considering different quantities of interest. The results are verified by available analytical solutions and validated by existing experimental data. Effect of material heterogeneity in the error distribution has also been investigated in several examples. Different quantities of interest result in various error distributions of that quantity and subsequently lead to different mesh configurations. The results have been compared with those obtained by other conventional mesh adaptivity procedures. The developed methodology leads to higher convergence rate and lower computational effort.

In conclusion, the proposed goal-oriented mesh adaptivity is a promising approach for obtaining highly accurate solution of a quantity of interest in a 3D elastoplasticity problem with optimal mesh configuration and minimal computational effort. Thus, this approach is highly recommended to be used for failure analysis of ductile material.

Keywords: Finite element method; Goal-oriented error estimation; Mesh adaptivity; Dual-weighted residual; Elastoplasticity; Von-Mises stress

Zusammenfassung

Die Entwicklung einer effizienten Adaptivitätsmethode für die Analyse von dreidimensionalen Elasto-Plastizitäts-Problemen mit dem Ziel der genauen Lösung einer interessierenden Zielgröße wird zunehmend gefordert. Die dreidimensionale Simulation eines elastoplastischen Materials ist ein bedeutendes Werkzeug im Ingenieurwesen und spielt eine wichtige Rolle in der Analyse und im Design von zahlreichen Anwendungen, zum Beispiel bei der Vorhersage von duktilem Versagen. Im Falle von nichtlinearen Problemen wird jedoch die Berechnungsdauer durch die einheitliche Verfeinerung des Netzes deutlich erhöht, besonders wenn sehr genaue Lösungen erforderlich sind. Demzufolge stellt eine Netzadaptivität, die auf einer zuverlässigen Fehlerabschätzungsmethode basiert, ein profitables Werkzeug dar.

Konventionelle Fehlerabschätzungsmethoden verwenden für die Genauigkeit bestimmter Größen, wie zum Beispiel Punktverschiebungen oder mittlere Spannungen in einem spezifischen Bereich, Energiefehlernormen. Zielorientierte Fehlerabschätzungsmethoden auf Basis dieser Normen sind in der Lage, den Lösungsfehler bezüglich der interessierenden Zielgröße abzuschätzen.

Die vorliegende Arbeit beschäftigt sich mit der Entwicklung eines neuartigen Netzadaptivitätverfahrens (unter Verwendung von Verfeinerung und Vergröberung) auf Basis einer zielorientierten Fehlerabschätzung für zweidimensionale Elastizitätsprobleme mit homogenen und heterogenen Materialien. Dieses Verfahren wurde zudem zum ersten Mal auf dreidimensionale Elastizitäts- und Elasto-Plastizitäts-Probleme erweitert.

Zu diesem Zweck wurden dual-gewichtete Residuen-Fehlerschätzungen, bei denen es sich um eine robuste zielorientierte Fehlerschätzung handelt, verwendet. Das ist ein dual-basiertes Verfahren, welches ein adjungiertes Problem mit der Definition einer Zielgröße erfordert. Nachfolgend werden elementweise geschätzte Fehler verwendet, um ein zielorierentiertes Netzadaptivitätsverfahren durchzuführen. Durch die Verwendung von Tetraeder- und Hexaeder-Elementen im Rahmen einer FEM-Analyse für zwei- und dreidimensionale Fälle werden hängende Knoten im Verfeinerungsprozess eingeführt. Diese sind eingeschränkt, um ihre Kompatibilität mit benachbarten Knoten zu gewährleisten.

Im vorliegenden Beitrag wird die Elasto-Plastizitäts-Analyse in beiden Fällen auf Basis einer Kraft- beziehungsweise Verformungskontrolle durchgeführt. Fehler in den Zielgrößen werden in jedem Kraft-Verformungs-Inkrement berechnet. Die Netzadaptivität auf Basis von Netzverfeinerung und -vergröberung wird berücksichtigt, wenn die Fehlernorm einen bestimmten Wert erreicht. Die Lösungen in den Knoten sowie die Zeitvariablen

an Gauss-Punkten werden übertragen und auf ein neues Netz nach jeder Netzadaption projektiert.

Dieses zielorientierte Netzadaptivitätsverfahren wird in verschiedenen zwei- und dreidimensionalen elastischen sowie elasto-plastischen numerischen Beispielen mit unterschiedlichen Zielgrößen angewendet. Die Ergebnisse werden verifiziert durch verfügbare analytische Lösungen und durch vorhandene experimentelle Daten validiert. Auswirkungen auf die Materialheterogenität in der Fehlerverteilung wurden ebenfalls an verschiedenen Beispielen untersucht. Unterschiedliche Zielgrößen in den jeweiligen Fehlerverteilungen der Zielgröße führen zu unterschiedlichen Netzkonfigurationen. Die Ergebnisse werden mit anderen Resultaten, die durch andere konventionelle Netzadaptivitätsverfahren erhalten wurden, verglichen. Die entwickelte Methode führt zu einer höheren Konvergenzrate und zu einem geringeren Berechnungsaufwand.

Zusammenfassend kann die vorgeschlagene zielorientierte Netzadaptivität als vielversprechendes Verfahren für die Gewinnung von sehr genauen Lösungen von Zielgrößen in dreidimensionalen Elasto-Plastizitätsproblemen unter Berücksichtigung einer optimalen Netzkonfiguration und minimalem Berechnungsaufwand verstanden werden. Demzufolge wird die Methode für die Verwendung bei der Versagensanalyse von duktilem Materialien empfohlen.

Schlagworte: Finite Elemente Methode; zielorientierte Fehlerabschätzung; Netzadaptivität; dual-gewichtete Residuen; Elastoplastizität; Von-Mises-Spannung

Acknowledgements

This research has been supported by the German Research Foundation (DFG) through Research Training Group 1462, which is gratefully acknowledged.

Firstly, I would like to express my sincere gratitude to my supervisor Prof. Dr.-Ing. Timon Rabczuk for the continuous support of my Ph.D. study and research, for his motivation, enthusiasm and immerse knowledge. I have gained a lot of information from his worthwhile comments.

Besides my supervisor, I would like to thank the rest of my thesis committee: Prof. Dr.-Ing. habil. Frank Werner, Prof. Stephane P.A. Bordas, Prof. Dr. rer. nat. habil. Klaus Gürlebeck, Dr. rer. nat. Sebastian Bock and Prof. Dr.-Ing. Karl Josef Witt for their encouragement and precious comments.

My sincere thanks also goes to Prof. Dr. rer. nat. Tom Lahmer for all the support and concern from my first working day in the research training group 1462.

I would like to express my sincere gratitude to Prof. Dr.-Ing. habil. Frank Werner. He is a very kind, experienced professor which supported me and all of the GRK members. I am so happy to have had the chance to get to know him and work closely with him.

Last but not the least, I am so grateful of my family for all their love and encouragement. For my parents who supported me in all my pursuits throughout my life. And most of all for my loving, supportive, encouraging, and patient wife Ghazal whose faithful support during the final stages of this Ph.D. is so appreciated.

Seyed Shahram Ghorashi
Weimar, July 2016

Contents

List of Figures

List of Tables

Abbreviations

DoF	**D**egree **o**f **F**reedom
DWR	**D**ual-**W**eighted **R**esidual
FEM	**F**inite **E**lement **M**ethod
GOEE	**G**oal-**O**riented **E**rror **E**stimation
PDE	**P**artial **D**ifferential **E**quation
QoI	**Q**uantity **o**f **I**nterest

Symbols

E	modulus of elasticity
$\mathbf{I}$	rank-2 unit symmetric tensor
$\mathbf{n}$	unit vector normal to the corresponding surface
$\mathbf{u}$	displacement vector
$\mathbf{u}^h$	approximated displacement vector (FEM solution)
$\mathbb{C}$	4^{t}h order material property tensor
$\mathbb{I}$	rank-4 identity tensor
μ	shear modulus
ν	Poisson's ratio
$\boldsymbol{\varepsilon}$	strain tensor
$\boldsymbol{\sigma}$	stress tensor

Chapter 1

Introduction

Nowadays, many challenging engineering problems are solved by numerical simulations. The Finite Element Method (FEM) [1, 2] is one of the most popular numerical approach. Although, many other computational approaches such as meshfree methods [3–6], isogeometric analysis method and its extensions [7–10] have been presented and successfully applied to a variety of problems, FEM is still most widely used in analysis and design of various stuctures in different fields like civil engineering and mechanical engineering.

For solving a problem, a mathematical model, Partial Differential Equation (PDE), should be chosen to represent the physical phenomenon and then FEM is utilized to solve it by discretizing the domain in finite dimensional spaces. Therefore, two main error types: model and discretization errors are incorporated into the final solution. In this contribution, approximating the discretization error is the major concern.

In the FEM, mesh discretization highly affects the solution accuracy and obviously the computational effort. Since simulation of complicated problems, especially nonlinear ones in three dimensions are computationally expensive, it is of great importance to be able to minimize the computational effort while the expected solution accuracy is gained.

Adaptivity methods are the keys to achieve this goal. Adaptive methods can be categorized into three different classes: h-, r- and p-adaptivity. In h-adaptivity the discretization is refined while p-adaptivity refers to locally increasing the polynomial order of the shape functions. R-adaptivity aims to find the optimal mesh topology for a given discretization. P-adaptivity is not well suited for problems involving localized deformation and plasticity since high gradients and localized deformation cannot be captured well with higher order. In this contribution, we consider h-adaptivity where the mesh is refined and coarsened based on the estimated element-wise errors.

A good error estimator plays a very important role to implement an efficient refinement procedure in numerical methods. An error estimate should be performed to locate the situations of error distribution in the problem domain. The error estimation methods based on classical energy norm are categorized into two broad classes namely residuals-based [11] and the recovery-based [12] error estimations. In the residual-based error estimations, which have a strong mathematical basis, the residuals of a governing differential equation and its boundary conditions are considered as an error criteria. On the other hand, in the recovery-based methods [13, 14] it is assumed that smoothed gradient of solution represent more realistic solution and the error is computed by taking their differences.

The conventional error estimation methods approximate errors in the energy norm. However, in many engineering applications other quantities are of major interest, e.g. the displacement at a point, mean stress in a region, load-deflection curve etc. One of the most important developments in error estimation in recent years is the discovery of methods entitled Goal-Oriented Error Estimation (GOEE) [15–23] for obtaining estimates of error in local quantity of interest. It results in quantifying the effect of local errors on the accuracy of the solution with respect to the specific quantities. Therefore, this methodology is so beneficial for adaptivity schemes and quality assessment in engineering applications.

Rannacher and Suttmeier have developed and applied the Dual-Weighted Residual (DWR) error estimation, which is a GOEE, to two dimensional linear elasticity and

elastic perfect plasticity problems [24–26]. Suttmeier extended his work later to plasticity with hardening and solved a 2d test example [27].

In many applications such as those in soil mechanics engineering, the material is not absolutely homogeneous, but rather heterogeneous. In such cases, the material properties can be regarded as random fields. This variety of material properties leads to non-uniform distributions of the solution gradients, e.g. stresses. Therefore, it is vital to apply a reliable error estimation approach in order to perform the mesh-adaptivity procedure efficiently with regard to varying material parameters with pre-defined correlation lengths.

Three-dimensional simulation of elastoplastic material is another important engineerng tool which plays a significant role in the analysis and design of numerous engineering applications, e.g. prediction of ductile failure. Since it is a nonlinear problem, its computational cost is notably increased by uniformly refining the mesh when highly accurate result is demanded. Accordingly, mesh adaptation based on a reliable error estimation method would be a profitable tool.

In this contribution, the Dual-Weighted Residual (DWR) error estimation is utilized as a guidance for mesh adaptivity process containing local refinement and coarsening. In the elastoplasticity problem an automatic continuous goal-oriented mesh adaptivity process is proposed by transferring and projecting the solution from an old mesh to a new mesh. For this purpose, the DWR error estimation, which was limited to 2d, is extended to 3d problems for both elasticity and elastoplasticity problems. The goal-oriented mesh adaptivity controls the local errors in terms of the prescribed quantity. Moreover, in this work the conventional residual-based error estimation and a recovery-based error estimation developed by Kelly et al. [28] have been implemented for the comparison purposes.

The proposed goal-oriented mesh adaptivity process has been applied to 2d elasticity problems with heterogeneous material distribution [29] and 3d homogeneous elasticity

[30] and elastoplasticity problems [31]. The 3d elastoplasticity FEM simulation accompanying the goal-oriented mesh adaptivity has been written in the C++ programming language within the framework of the deal.II library [32, 33] and is available online as an opensource code. It smooths the way for its application and further development.

Several numerical simulations are performed and the results are compared with available analytical solutions, existing experimental data and the results of mesh adaptivity based on other typical error estimation methods.

The remainder of the thesis is structured as follows: Chapter 2 describes the finite element method (FEM) formulations for solving an elasticity and elastoplasticity problems. Two conventional error estimation methods applied in this work are presented in Chapter 3. It is followed by introducing and describing the goal-oriented error estimation (GOEE) in Chapter 4. Afterwards, Chapter 5 depicts the mesh adaptivity procedure. Subsequently, by investigating the proposed approach in several numerical examples in Chapter 6, concluding remarks are given in Chapter 7.

Chapter 2

Finite Element Method

Physical phenomena in engineering applications are modeled as mathematical models including partial differential equations in space and time. In general, analytical solutions of these equations do not exist, hence numerical methods are employed. The finite element method is one of the most powerful numerical techniques available for finding approximate solutions to boundary value problems for partial differential equations. It uses subdivision of a whole problem domain into simpler parts, called finite elements, and variational methods from the calculus of variations to solve the problem by minimizing an associated error function. Analogous to the idea that connecting many tiny straight lines can approximate a larger circle, FEM encompasses methods for connecting many simple element equations over many small subdomains, named finite elements, to approximate a more complex equation over a larger domain.

In the following the FEM procedure for solving elasticity and elastoplasticty problems are described.

2.1 Linear elasticity

Linear elasticity is a mathematical model for representing the material behavior (deformation and internal stresses) with the following assumptions:

- The material deforms reversibly: The solid returns to its original shape by removing the loads.
- The strain in the solid object is infinitesimal: Deformations are too small compared to the body dimensions.
- The strain depends only on the applied loads and not on the rate or history of loading.
- The stress is a linear function of strain.

Linear elasticity is only applicable for stress states that do not result in yielding.

2.1.1 Governing equations

Let us consider the following equilibrium equation in the elasticity problem:

$$-\nabla \cdot \boldsymbol{\sigma} = \mathbf{f} \quad \text{in } \Omega\,, \tag{2.1}$$

in a domain $\Omega \subset \mathbb{R}^d$ (d denotes the dimension size). $\mathbf{f}$ represents the external force vector. Stress tensor $\boldsymbol{\sigma}$ is defined as

$$\boldsymbol{\sigma} = \mathbb{C}^e : \boldsymbol{\varepsilon}(\mathbf{u})\,, \tag{2.2}$$

where $\mathbb{C}^e$ is the fourth-order material property tensor which can be written as a function of shear modulus μ and bulk modulus κ in the following form:

$$\mathbb{C}^e = 2\mu(\mathbb{I} - \mathbf{I} \otimes \mathbf{I}) + \kappa \mathbf{I} \otimes \mathbf{I}\,, \tag{2.3}$$

where $\mathbf{I}$ is the rank-2 unit symmetric tensor and $\mathbb{I}$ is the rank-4 identity tensor. The shear modulus μ and bulk modulus κ can be written in the form of elasticity modulus E and Poisson's ratio ν

$$\mu = \frac{E}{2(1+\nu)}\,, \tag{2.4}$$

$$\kappa = \frac{E}{3(1-2\nu)}\,. \tag{2.5}$$

Strain tensor $\boldsymbol{\varepsilon}$ in Eq. (2.2) is calculated by taking the symmetric gradient of the displacement vector $\mathbf{u}$,

$$\boldsymbol{\varepsilon}(\mathbf{u}) = \frac{1}{2}\left(\nabla\mathbf{u} + (\nabla\mathbf{u})^T\right)\,. \tag{2.6}$$

The Dirichlet and Neumann boundary conditions can be written as

$$\mathbf{u} = \bar{\mathbf{u}} \quad \text{on } \Gamma_u\,, \tag{2.7}$$

$$\boldsymbol{\sigma}\cdot\mathbf{n} = \bar{\mathbf{t}} \quad \text{on } \Gamma_n\,. \tag{2.8}$$

where $\bar{\mathbf{u}}$ and $\bar{\mathbf{t}}$ are prescribed displacement and traction imposed on the boundaries Γ_u and Γ_n, respecively.

2.1.2 Variational form

By multiplying Eq. (2.1) by a test function and integrating by parts, the following weak/variational formulation is obtained

$$a(\mathbf{u}, \mathbf{v}) = f(\mathbf{v}), \qquad \mathbf{u} \in \mathbf{V}, \forall \mathbf{v} \in \mathbf{V}_0\,, \tag{2.9}$$

where

$$\mathbf{V} = \{\mathbf{u} \in \left[H^1(\Omega)\right]^d\}\,. \tag{2.10}$$

The bilinear form is written as

$$a(\mathbf{u}, \mathbf{v}) = (\mathbb{C}^e : \boldsymbol{\varepsilon}(\mathbf{u}), \boldsymbol{\varepsilon}(\mathbf{v}))\,, \tag{2.11}$$

and

$$f(\mathbf{v}) = (\mathbf{f}, \mathbf{v}) + (\overline{\mathbf{t}}, \mathbf{v})_{\Gamma_n}\,, \tag{2.12}$$

is a bounded linear functional in the space

$$\mathbf{V}_0 = \{\mathbf{v} \in \left[H^1(\Omega)\right]^d : \mathbf{v} = 0 \text{ on } \Gamma_d\}\,. \tag{2.13}$$

2.1.3 Discretization

In order to compute the Eq. (2.9) numerically, the problem domain is descretized into $\mathbb{T}_h$ meshes. Subsequently, by considering the subspace $\mathbf{V}_0^h \subset \mathbf{V}_0$, the following Galerkin equation is solved to calculate the finite element solution $\mathbf{u}^h$,

$$a(\mathbf{u}^h, \mathbf{v}^h) = f(\mathbf{v}^h) \qquad \forall \mathbf{v}^h \in \mathbf{V}_0^h\,. \tag{2.14}$$

2.2 Elastoplasticity

Elastoplastic problems are commonly presented as partial differential equations with an inequality as a result of the material plasticity.

2.2.1 Governing equations

The governing equations for calculating the displacement field $\mathbf{u} \in \mathbf{V} := \{\mathbf{v} \in \left[H^1(\Omega)\right]^d\}$, stress tensor $\boldsymbol{\sigma}$ and plastic strain tensor $\boldsymbol{\varepsilon}^p$ in a domain $\Omega \subset \mathbb{R}^d$ (d denotes the dimension which can be 2 or 3 in our computations) are described.

- Equilibrium equation:

$$-\nabla \cdot \boldsymbol{\sigma} = \mathbf{f}\,, \quad \text{in } \Omega\,. \tag{2.15}$$

- Relationship between strain $\boldsymbol{\varepsilon}(\mathbf{u}) = \frac{1}{2}\left(\nabla\mathbf{u} + (\nabla\mathbf{u})^T\right)$ and stress σ:

$$\boldsymbol{\sigma} = \mathbb{C}^e : (\boldsymbol{\varepsilon}(\mathbf{u}) - \boldsymbol{\varepsilon}^p)\,, \tag{2.16}$$

  where $\mathbb{C}^e$ is the fourth-order material property tensor in the elastic case.

- Complementarity condition:

$$\boldsymbol{\varepsilon}^p : (\boldsymbol{\tau} - \boldsymbol{\sigma}) \geq 0\,, \quad \forall \boldsymbol{\tau} \text{ with } F(\boldsymbol{\tau}, \sigma_y) \leq 0\,. \tag{2.17}$$

  where τ is in the admissible stress space; σ_y denotes the yield stress. Note that $\boldsymbol{\varepsilon}^p = 0$ if $F(\boldsymbol{\sigma}, \sigma_y) < 0$ and $\boldsymbol{\varepsilon}^p$ may be a nonzero tensor if and only if $F(\boldsymbol{\sigma}, \sigma_y) = 0$. The above complementarity condition can be reformulated as equality using the Chen-Mangasarian replacement functions [34–36].

- Essential boundary condition:

$$\mathbf{u} = \bar{\mathbf{u}}\,, \quad \text{on } \Gamma_u\,. \tag{2.18}$$

- Natural (Neumann) boundary condition:

$$\boldsymbol{\sigma} \cdot \mathbf{n} = \bar{\mathbf{t}}\,, \quad \text{on } \Gamma_n\,. \tag{2.19}$$

where $\bar{\mathbf{u}}$ and $\bar{\mathbf{t}}$ are prescribed displacement and traction imposed on the boundaries Γ_u and Γ_n, respecively.

2.2.2 Flow function

The internal stresses $\boldsymbol{\sigma}(\mathbf{x})$ are restricted to some maximal stress, i.e. that fulfilles an inequality $F(\boldsymbol{\sigma}, \sigma_y) \leq 0$ at every point $\mathbf{x}$. A sample of such a function is the von Mises flow function $F(\boldsymbol{\sigma}, \sigma_y) = \sigma_v - \sigma_y$ where

$$\sigma_v = \sqrt{3J_2} = \sqrt{\frac{3}{2}}\left|\boldsymbol{\sigma}^D\right|\,, \tag{2.20}$$

is the von Mises stress; J_2 is the second deviotoric stress invariant,

$$J_2 = \frac{1}{2}\sum_{i,j=1}^{d}\left(\sigma_{ij}^D\right)^2\,, \tag{2.21}$$

and $\boldsymbol{\sigma}^D = \boldsymbol{\sigma} - \frac{1}{3}tr(\boldsymbol{\sigma})\mathbf{I}$ is the deviatoric part of stress tensor; $|\boldsymbol{\sigma}^D|$ denotes the Frobenius norm of deviatoric stress,

$$|\boldsymbol{\sigma}^D| = \left(\sum_{i,j=1}^{d}\left(\sigma_{ij}^D\right)^2\right)^{1/2}\,. \tag{2.22}$$

If the von Mises stress, σ_v, tends to σ_y, the material stops behaving elastically and plastic yielding occurs. A popular flow rule for such material, e.g. Aluminium, is von Mises flow function considering linear isotropic hardening law,

$$\sigma_y = \sigma_0 + \gamma^{\text{iso}} \left|\boldsymbol{\varepsilon}^p\right| , \tag{2.23}$$

where $\gamma^{\text{iso}} > 0$ is the isotropic hardening parameter.

2.2.3 Constitutive law

By applying a projector onto the set of admissible stresses, a primal problem can be formulated [27]. For the case of isotropic media with linear isotropic hardening, the 4^{th} order material property tensor is defined as [37]

$$\mathbb{C} = \mathbb{C}(\boldsymbol{\varepsilon}(\mathbf{u})) = \begin{cases} \mathbb{C}_\mu + \mathbb{C}_\kappa \,, & \sigma_v \leq \sigma_0 \,, \\ \mathbb{C}_\mu[\gamma + (1-\gamma)\frac{\sigma_0}{\sigma_v}] + \mathbb{C}_\kappa \,, & \sigma_v > \sigma_0 \,, \end{cases} \tag{2.24}$$

where

$$\mathbb{C}_\mu = 2\mu(\mathbb{I} - \mathbf{I}\otimes\mathbf{I}), \qquad \mathbb{C}_\kappa = \kappa\mathbf{I}\otimes\mathbf{I}\,. \tag{2.25}$$

$\mathbf{I}$ is the rank-2 unit symmetric tensor and $\mathbb{I}$ is the rank-4 identity tensor; μ and κ are the shear modulus and bulk modulus, respectively.

By applying Eq. (2.24), the stress tensor can be calculated as

$$\boldsymbol{\sigma} = \mathbb{C}(\boldsymbol{\varepsilon}(\mathbf{u})) : \boldsymbol{\varepsilon}(\mathbf{u})\,. \tag{2.26}$$

For computing σ_v in Eq. (2.24), the elasticity formulation is assumed, $\mathbb{C}^e = \mathbb{C}_\mu + \mathbb{C}_\kappa$.

2.2.4 Variational form

For the elastoplasticity problem, the primal variational formulation has the following nonlinear form

$$a(\mathbf{u})(\mathbf{v}) = f(\mathbf{v})\,, \qquad \mathbf{u} \in \mathbf{V}, \forall \mathbf{v} \in \mathbf{V}_0\,, \tag{2.27}$$

with

$$a(\mathbf{u})(\mathbf{v}) = (\mathbb{C} : \boldsymbol{\varepsilon}(\mathbf{u}), \boldsymbol{\varepsilon}(\mathbf{v}))\,, \tag{2.28}$$

$$f(\mathbf{v}) = (\mathbf{f}, \mathbf{v}) + (\overline{\mathbf{t}}, \mathbf{v})_{\Gamma_n}\,, \tag{2.29}$$

in the space

$$\mathbf{V}_0 = \{\mathbf{v} \in \left[H^1(\Omega)\right]^d : \mathbf{v} = 0 \ \text{ on } \Gamma_d\} \tag{2.30}$$

2.2.5 Newton linearization

In order to solve the primal formulation (2.27), a damped Newton method is applied.

Firstly, linearization should be performed and a method similar to the frequently used radial-return mapping algorithm [37, 38] is adopted.

In Newton scheme, solution is updated at each iteration, $\Delta\mathbf{U}_{n+1}^{k+1} = \Delta\mathbf{U}_{n}^{k+1} + \alpha_{n+1}\delta\mathbf{U}_{n+1}^{k+1}$. α_{n+1} is called step length and can be calculated when the $\delta\mathbf{U}_{n+1}^{k+1}$ is known. As a

result, we derive the equations for $\delta\mathbf{U}_{n+1}^{k+1}$ supposing that $\alpha_{n+1} = 1$. Consequently, $\delta\mathbf{U}_{n+1}^{k+1} = \Delta\tilde{\mathbf{U}}_{n+1}^{k+1} - \Delta\mathbf{U}_{n}^{k+1}$ can be calculated.

By Applying the full Newton method, the following equation needs to be solved at each load/displacement increment k and Newton iteration n:

$$\begin{aligned}\left(\mathbb{C}^{lin}(\boldsymbol{\varepsilon}_n^{k+1})\Delta\boldsymbol{\varepsilon}(\Delta\tilde{\mathbf{u}}_{n+1}^{k+1}), \boldsymbol{\varepsilon}(\mathbf{v})\right) &= \left(f^{k+1}, \mathbf{v}\right) - \left(\boldsymbol{\sigma}_n^{k+1}, \boldsymbol{\varepsilon}(\mathbf{v})\right) \\ &\quad + \left(\mathbb{C}^{lin}(\boldsymbol{\varepsilon}_n^{k+1})\Delta\boldsymbol{\varepsilon}_n^{k+1}, \boldsymbol{\varepsilon}(\mathbf{v})\right),\end{aligned} \tag{2.31}$$

where $\mathbb{C}^{lin}(\varepsilon)$ denotes the linearization of the material property tensor (Eq. (2.24)) around $\boldsymbol{\varepsilon}^D(\mathbf{u}_n^{k+1})$ [37],

$$\mathbb{C}^{lin} = \mathbb{C}^{lin}(\boldsymbol{\varepsilon}(\mathbf{u})) = \begin{cases} \mathbb{C}_\mu + \mathbb{C}_\kappa\,, & \sigma_v \le \sigma_0\,, \\ \mathbb{C}_\mu[\gamma + (1-\gamma)\frac{\sigma_0}{\sigma_v}] + \mathbb{C}_\kappa & \\ -2\mu(1-\gamma)\frac{\sigma_0}{\sigma_v}(\frac{\boldsymbol{\sigma}^D}{|\boldsymbol{\sigma}^D|} \otimes \frac{\boldsymbol{\sigma}^D}{|\boldsymbol{\sigma}^D|})\,, & \sigma_v > \sigma_0\,. \end{cases} \tag{2.32}$$

The initial solution field is considered zero,

$$\mathbf{U}^0 = 0, \quad \Delta\mathbf{U}_0^{k+1} = 0\,, \tag{2.33}$$

and the initial history stress and strain field, which are stored at the Gauss points, are defined as

$$\boldsymbol{\sigma}^0 = 0, \quad \boldsymbol{\varepsilon}^0 = 0, \quad \boldsymbol{\sigma}_0^{k+1} = \boldsymbol{\sigma}^k\,.$$

By applying Eq. (2.31) and using line search method (Sec. 2.2.6), $\Delta\mathbf{U}_{n+1}^{k+1}$ is computed. Then, $\Delta\boldsymbol{\varepsilon}_{n+1}^{k+1}$ can be calculated by taking its symmetric gradient,

$$\Delta\boldsymbol{\varepsilon}_{n+1}^{k+1} = \nabla^{\mathrm{sym}}(\Delta\mathbf{u}_{n+1}^{k+1})\,. \tag{2.34}$$

yielding subsequently

$$\boldsymbol{\varepsilon}_{n+1}^{k+1} = \boldsymbol{\varepsilon}^{k} + \Delta\boldsymbol{\varepsilon}_{n+1}^{k+1}\,, \tag{2.35}$$

$$\boldsymbol{\sigma}_{n+1}^{k+1} = \mathbb{C}(\boldsymbol{\varepsilon}_{n+1}^{k+1})\boldsymbol{\varepsilon}_{n+1}^{k+1}\,. \tag{2.36}$$

Then, we can start the next iteration if the convergence criterion is not satisfied, otherwise the solution field, $\mathbf{U}^{k+1}$, and history fields, $\boldsymbol{\sigma}^{k+1}$, $\boldsymbol{\varepsilon}^{k+1}$, are updated and we can start the next increment procedure.

$$\mathbf{U}^{k+1} = \mathbf{U}^{k} + \Delta\mathbf{U}_{n+1}^{k+1}\,. \tag{2.37}$$

2.2.6 Line search

In order to make the Newton method more robust, we globalize it by a damping parameter applying the line search method [39].

After computing $\Delta\tilde{\mathbf{U}}_{n+1}^{k+1}$ by using Eq. (2.31), line search is applied to determine $\Delta\mathbf{U}_{n+1}^{k+1}$ for the next Newton iteration. We apply the backtracking line search [40] to find the first step length $\alpha_{n+1} \in \{1, 2^{-1}, 2^{-2}, \ldots\}$ so that

$$\left\| R(\mathbf{U}^{k} + \Delta\mathbf{U}_{\alpha}) \right\|_{l_2} < \left\| R(\mathbf{U}^{k} + \Delta\mathbf{U}_{n}^{k+1}) \right\|_{l_2}\,, \tag{2.38}$$

where $\Delta\mathbf{U}_\alpha = (1-\alpha_{n+1})\Delta\mathbf{U}_n^{k+1} + \alpha_{n+1}\Delta\tilde{\mathbf{U}}_{n+1}^{k+1}$.

$R(\mathbf{u})$ denotes the nonlinear residual,

$$R(\mathbf{u}) = a(\mathbf{u})(\mathbf{v}) - f(\mathbf{v})\,. \tag{2.39}$$

Fig. 2.1 demonstrates the general algorithm of the applied damped Newton procedure at the $(k+1)^{\text{th}}$ load/displacement increment.

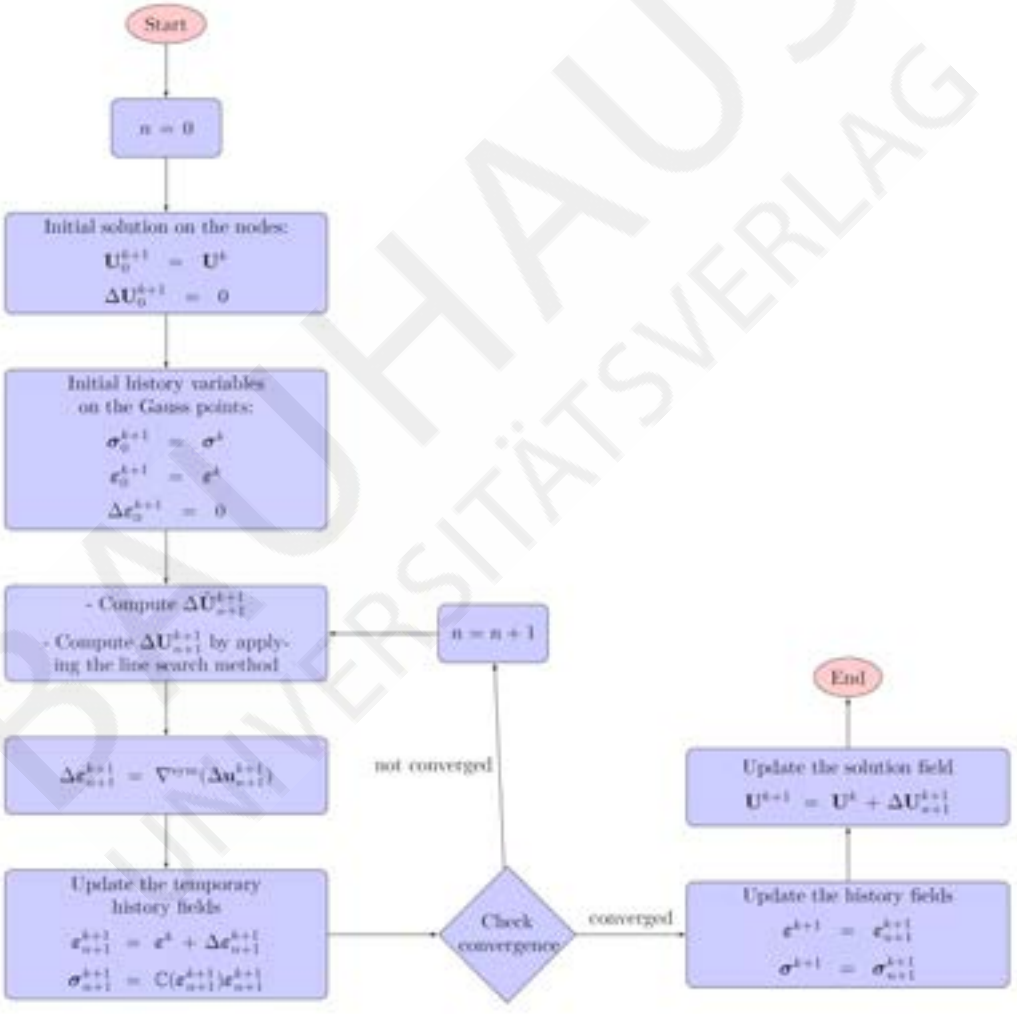

FIGURE 2.1: General algorithm of damped Newton process at the load/displacement increment $k+1$.

Chapter 3

Error Estimation

The finite element method involves different sources of numerical errors [41]. The focus of this thesis is only on the discretization error which is due to the finite element (polynomial) approximation of the solution. Hence, we assume that an appropriate mathematical model has been chosen and, even for this case, we are only concerned with one specific error, namely the discretization error arising in the finite element solution of this model.

There exist different types of discretization error estimates, including residuals-based [11] and the recovery-based [12, 28] error estimations. While a residual-based error estimator, applies the residuals of a governing differential equation and its boundary conditions as an error criteria, recovery-based methods [13, 14] utilize the gradient of solutions. For detailed reviews of the existing error estimations and their classifications, interested readers are referred to [42, 43].

In this contribution, a recovery-based error estimation developed by Kelly et al. [28] and a residual-based error estimation (based on edge and element residuals) are applied to be able to compare the results of goal-oriented error estimation (see Chapter 4) with those obtained by applying conventional error estimations. These are described in the following sections.

3.1 Kelly error estimation

This error indicator [28] tries to approximate the error per element by integration of the jump of the gradient of the solution along the faces of each element. It can be understood as a gradient recovery estimator; see the survey [42] for a complete discussion.

It is noted that in spite of the name, this is not truly an a posteriori error estimator. It gives good hints for mesh refinement, but the estimate is not to be trusted. For higher order trial spaces the integrals computed here tend to zero faster than the error itself, thus ruling out the values as error estimators.

The error estimator really only estimates the error for the generalized Poisson's equation $-\nabla \cdot a(\mathbf{x})\nabla \mathbf{u} = \mathbf{f}$ with either Dirichlet boundary conditions or generalized Neumann boundary conditions involving the conormal derivative $a\frac{\partial \mathbf{u}}{\partial \mathbf{n}} = \mathbf{g}$.

At each element K, the error is calculated as follow

$$\eta_K^2 = \frac{h}{24} \int_{\partial K} \left[\frac{\partial \mathbf{u}^h}{\partial \mathbf{n}} \right]^2 ds \,, \tag{3.1}$$

where $[\cdot]$ denotes the jump of the argument at the element face. h is taken to be the greatest length of the diagonals of the element. For more or less uniform elements without deformed angles, this coincides with the diameter of the cell. In the paper [42], h is divided by 24, but this factor is a bit esoteric, stemming from interpolation estimates and stability constants which may hold for the Poisson's problem, but may not hold for more general situations. In the implementation, this factor is considered, but may lead to wrong results and scaling appropriately the vector afterwards may be needed.

This approach has been applied since it is fast and straightforward to implement and practically useful for mesh adaptation process.

3.2 Residual-based error estimation

The applied residual-based error estimator is an explicit a posteriori one which involves a direct computation of the interior element residuals and the jumps at the element boundaries to find an estimate for the error in the energy norm, see [11]. By discretizing the domain into $\mathbb{T}_h$ meshes and calculating the FEM solution $\mathbf{u}^h$, the starting point racalling the Eq. (2.9) is the error representation

$$a(\mathbf{e}^h, \mathbf{v}) = f(\mathbf{v}) - a(\mathbf{u}^h, \mathbf{v}), \qquad \forall \mathbf{v} \in \mathbf{V}_0\,. \tag{3.2}$$

If the domain integral is split into the contributions from each element, Eq. (3.2) can be rewritten for the elasticity problem as

$$a(\mathbf{e}^h, \mathbf{v}) = \sum_{K \in \mathbb{T}_h} \{(\mathbf{f}, \mathbf{v})_K + (\overline{\mathbf{t}}, \mathbf{v})_{\partial K \cap \Gamma_n} - (\mathbb{C}^e : \boldsymbol{\varepsilon}(\mathbf{u}^h), \boldsymbol{\varepsilon}(\mathbf{v}))_K\}\,, \tag{3.3}$$

where K denotes the volume of an element in $\mathbb{T}_h$ and ∂K denotes its boundary. Applying integration by parts to the last term in Eq. (3.3) and rearranging terms leads to

$$a(\mathbf{e}^h, \mathbf{v}) = \sum_{K \in \mathbb{T}_h} \{(\mathbf{R}^h, \mathbf{v})_K + (\mathbf{r}^h, \mathbf{v})_\Gamma\}\,, \tag{3.4}$$

where $\mathbf{R}^h$ is the interior element residual

$$\mathbf{R}^h|_k = \mathbf{f} + \nabla \cdot \boldsymbol{\sigma} = \mathbf{f} + \nabla \cdot (\mathbb{C}(\boldsymbol{\varepsilon}(\mathbf{u}^h))\, \boldsymbol{\varepsilon}(\mathbf{u}^h))\,. \tag{3.5}$$

and $\mathbf{r}^h$ is the jump of the gradient across the element edge Γ

$$\mathbf{r}^h|_\Gamma = \begin{cases} \frac{1}{2}\mathbf{n}\cdot[\mathbb{C}(\boldsymbol{\varepsilon}(\mathbf{u}^h))\boldsymbol{\varepsilon}(\mathbf{u}^h)]\,, & \text{if } \Gamma \subset \partial K \setminus \partial\Omega\,, \\ \bar{\mathbf{t}} - \mathbf{n}\cdot\mathbb{C}(\boldsymbol{\varepsilon}(\mathbf{u}^h))\boldsymbol{\varepsilon}(\mathbf{u}^h)\,, & \text{if } \Gamma \subset \Gamma_n\,, \\ 0\,, & \text{if } \Gamma \subset \partial\Omega \setminus \Gamma_n\,. \end{cases} \tag{3.6}$$

By utilizing the Galerkin orthogonality condition and Cauchy-Schwarz inequality, the following a posteriori error estimate is deriven:

$$\|\mathbf{e}\|_E \leq C \left(\sum_{K\in\mathbb{T}_h} \{h_K^2 \|\mathbf{R}^h\|^2_{L_2(K)} + h_K \|\mathbf{r}^h\|^2_{L_2(\partial K)}\} \right)^{1/2}, \tag{3.7}$$

where $\|\cdot\|_E$ denotes the energy norm for the model problem $\|\mathbf{v}\|_E^2 = a(\mathbf{v},\mathbf{v})$. Apart from the constant C, all of the quantities on the right-hand can be computed explicitly from the data and the finite element approximation; h_K is the diameter of the element K. The purpose in doing so is that defining the local error indicator by η_K on element K by

$$\eta_K^2 = h_K^2 \|\mathbf{R}^h\|^2_{L_2(K)} + h_K \|\mathbf{r}^h\|^2_{L_2(\partial K)}\,, \tag{3.8}$$

allows one to identify contributions from each of the elements. It is then assumed that each of these quantities is a measure of the local discretization error over each element. In this way one can use η_K as a basis for guiding local mesh refinements.

The edge residual, $\mathbf{r}^h|_\Gamma$, in Eq. (3.6) is obtained by exchanging half of the edge integral of element K with the neighbor element K' and considering the opposite sign of their normal vectors. It can be rewritten in the index form using the Einstein notation as follow

$$r_i^h \mid_{\partial K} = \begin{cases} \frac{1}{2}\left(C_{ijkl}\varepsilon_{kl}(\mathbf{u}^h) \mid_K - C_{ijkl}\varepsilon_{kl}(\mathbf{u}^h) \mid_{K'}\right) n_j\,, & \text{if } \Gamma \subset \partial K \setminus \partial\Omega\,, \\ \bar{t}_i - \left(C_{ijkl}\varepsilon_{kl}(\mathbf{u}^h)\right) n_j\,, & \text{if } \Gamma \subset \Gamma_n\,, \\ 0\,, & \text{if } \Gamma \subset \Gamma_d\,. \end{cases} \tag{3.9}$$

where $i, j, k, l = 1, \ldots, d$ with the dimension size d. Correspondingly, the Eq. (3.5), can be rewritten in the following form

$$\begin{aligned} R_i^h \mid_k &= f_i + \partial_{x_j}\sigma_{ij}\,, \\ &= f_i + \partial_{x_j}\left(\mathbb{C}_{ijkl}\varepsilon_{kl}(\mathbf{u}^h)\right)\,, \\ &= f_i + \partial_{x_j} C_{ijkl}\,\varepsilon_{kl}(\mathbf{u}^h) + C_{ijkl}\,\partial_{x_j}\varepsilon_{kl}(\mathbf{u}^h)\,. \end{aligned} \tag{3.10}$$

According to the definition of the strain, the last term of the above equation can be written as

$$\begin{aligned} \partial_{x_j}\varepsilon_{kl}(\mathbf{u}^h) &= \frac{1}{2}\partial_{x_j}\left(\partial_l u_k^h + \partial_k u_l^h\right)\,, \\ &= \frac{1}{2}\left(\partial_{x_j}\partial_l u_k^h + \partial_{x_j}\partial_k u_l^h\right)\,. \end{aligned} \tag{3.11}$$

We can derive the $\partial_{x_j}\mathbb{C}$ in Eq. (3.10), considering the Eq. (2.24):

$$\partial_{x_j}\mathbb{C} = \begin{cases} 0\,, & \sigma_v \le \sigma_0\,, \\ \mathbb{C}_\mu(1-\gamma)\sigma_0\partial_{x_j}\left(\frac{1}{\sqrt{\frac{3}{2}|\boldsymbol{\sigma}^D|}}\right)\,, & \sigma_v > \sigma_0\,. \end{cases} \tag{3.12}$$

For deriving the $\partial_{x_j}\left(\frac{1}{|\boldsymbol{\sigma}^D|}\right)$, let us recall some known equations:

$|\boldsymbol{\sigma}^D|$ is the Frobenius norm of the deviatoric part of the stress in elastic case,

$$\begin{aligned} \boldsymbol{\sigma} &= \mathbb{C}_\mu \boldsymbol{\varepsilon}(\mathbf{u}^h) + \mathbb{C}_\kappa \boldsymbol{\varepsilon}(\mathbf{u}^h) \\ &= 2\mu \boldsymbol{\varepsilon}^D(\mathbf{u}^h) + \kappa tr(\boldsymbol{\varepsilon}(\mathbf{u}^h))\mathbb{I} \\ &= 2\mu \left(\boldsymbol{\varepsilon}(\mathbf{u}^h) - \frac{1}{d} tr(\boldsymbol{\varepsilon}(\mathbf{u}^h))\mathbb{I} \right) + \kappa tr(\boldsymbol{\varepsilon}(\mathbf{u}^h))\mathbb{I}\,, \end{aligned} \tag{3.13}$$

Therefore,

$$tr(\boldsymbol{\sigma}) = 0 + d\,\kappa\, tr(\boldsymbol{\varepsilon}(\mathbf{u}^h))\,, \tag{3.14}$$

$$\boldsymbol{\sigma}^D = \boldsymbol{\sigma} - \frac{1}{d} tr(\boldsymbol{\sigma})\mathbf{I} = 2\mu \left(\boldsymbol{\varepsilon}(\mathbf{u}^h) - \frac{1}{d} tr(\boldsymbol{\varepsilon}(\mathbf{u}^h))\mathbf{I} \right)\,, \tag{3.15}$$

$$|\boldsymbol{\sigma}^D| = 2\mu \left(\sum_{i,j=1}^{d} \left(\varepsilon_{ij}(\mathbf{u}^h) - \frac{1}{d} tr(\boldsymbol{\varepsilon}(\mathbf{u}^h))\delta_{ij} \right)^2 \right)^{1/2} = 2\mu |\boldsymbol{\varepsilon}^D(\mathbf{u}^h)|\,. \tag{3.16}$$

By applying the Eq. (3.16), we have

$$
\begin{aligned}
\partial_{x_j}\left(\frac{1}{|\boldsymbol{\sigma}^D|}\right) &= \partial_{x_j}\left(\frac{1}{2\mu|\boldsymbol{\varepsilon}^D(\mathbf{u}^h)|}\right) \\
&= \frac{1}{2\mu}\partial_{x_j}\left(\sum_{k,l=1}^{d}\left(\varepsilon_{kl}^D(\mathbf{u}^h)\right)^2\right)^{-1/2} \\
&= \frac{1}{2\mu}\cdot\frac{-1}{2}\left(\sum_{k,l=1}^{d}\left(\varepsilon_{kl}^D(\mathbf{u}^h)\right)^2\right)^{-3/2}\sum_{k,l=1}^{d}\left(2\varepsilon_{kl}^D(\mathbf{u}^h)\partial_{x_j}\varepsilon_{kl}^D(\mathbf{u}^h)\right) \\
&= \frac{-1}{2\mu}\frac{1}{|\boldsymbol{\varepsilon}^D(\mathbf{u}^h)|^3}\sum_{k,l=1}^{d}\left(\varepsilon_{kl}^D(\mathbf{u}^h)\partial_{x_j}\varepsilon_{kl}^D(\mathbf{u}^h)\right), \qquad (3.17)
\end{aligned}
$$

where

$$
\begin{aligned}
\partial_{x_j}\varepsilon_{kl}^D(\mathbf{u}^h) &= \partial_{x_j}\left(\varepsilon_{kl}(\mathbf{u}^h) - \frac{1}{d}tr(\boldsymbol{\varepsilon}(\mathbf{u}^h))\delta_{kl}\right) \\
&= \partial_{x_j}\varepsilon_{kl}(\mathbf{u}^h) - \frac{1}{d}\sum_{i=1}^{d}\{\partial_{x_j}\varepsilon_{ii}(\mathbf{u}^h)\}\delta_{kl}\,. \qquad (3.18)
\end{aligned}
$$

Then, by applying the Eq. (3.17), Eq. (3.12) can be rewritten as follows:

$$
\partial_{x_j}\mathbb{C} = \begin{cases} 0\,, & \sigma_v \le \sigma_0\,, \\ \frac{-\mathbb{C}_\mu(1-\gamma)\sigma_0}{\sqrt{\frac{3}{2}}2\mu|\boldsymbol{\varepsilon}^D(\mathbf{u}^h)|^3}\sum_{k,l=1}^{d}\left(\varepsilon_{kl}^D(\mathbf{u}^h)\partial_{x_j}\varepsilon_{kl}^D(\mathbf{u}^h)\right), & \sigma_v > \sigma_0\,. \end{cases} \qquad (3.19)
$$

and finally, the element residuals, Eq. (3.10), can be calculated.

Chapter 4

Goal-Oriented Error Estimation

In engineering applications the entire solution of the problem may not be interested, but rather some certain aspects of it. For example, in an elasticity problem one might want to know about values of the stress at certain points to predict whether maximal load values of joints are safe.

Goal-oriented error estimation (GOEE) methods have been developed to estimate the error in a quantity of interest [15–23], e.g. displacement at a point or the average stress over a region. In GOEE besides the main (primal) problem, the solution of a dual/auxiliary problem is required.

4.1 Primal problem

The primal problem is the main problem defined in Eq. (2.27). By discretizing the domain into finite elements, the following variational formulation is obtained

$$a(\mathbf{u}^h)(\mathbf{v}^h) = f(\mathbf{v}^h) \qquad \forall \mathbf{v}^h \in \mathbf{V}_0^h \,. \tag{4.1}$$

with subspaces $\mathbf{V}_0^h \subset \mathbf{V}_0$.

4.2 Dual problem

The Quantity of Interest (QoI) can be described as a continuous linear functional, $J(\mathbf{u})$, on the space of admissible functions. If the QoI functional is non-linear, it may be linearized and then be used [21, 44]. Sometimes the functional may not be continuous, for instance, when we seek the solution error at a particular point in the domain. Therefore, the evaluation of a QoI functional, $J(\mathbf{u})$, is of interest rather than the solution values, $\mathbf{u}$, in the entire domain. The GOEE approximates the error in the QoI, $J(\mathbf{e}) = J(\mathbf{u}) - J(\mathbf{u}^h)$.

In the following, the main formulations are firstly given for the elasticity problem, then the corresponding equations are extracted for the elastoplasticity problem.

4.2.1 Elasticity problem

The dual problem for the elasticity problem is written in the form [24, 30]

$$a(\mathbf{v}, \mathbf{z}) = J(\mathbf{v}) \qquad \forall \mathbf{v} \in \mathbf{V}_0 \,, \tag{4.2}$$

where $a(\cdot, \cdot)$ is the bi-linear form associated with the elasticity problem (so-called energy form)

$$a(.,.) = (\mathbb{C} : \boldsymbol{\varepsilon}(.), \boldsymbol{\varepsilon}(.)), \tag{4.3}$$

and $\mathbf{z}$ denotes the solution. Then, by considering $\mathbf{v} = \mathbf{e} = \mathbf{u} - \mathbf{u}^h$ as the error, we have

$$J(\mathbf{e}) = a(\mathbf{e}, \mathbf{z}) \,, \tag{4.4}$$

which it can be rewritten in the following form by applying the Galerkin orthogonality,

$$J(\mathbf{e}) = a(\mathbf{e}, \mathbf{z} - \mathbf{z}^h) = a\left(\mathbf{e}, \mathbf{e}^Q\right) , \tag{4.5}$$

where $\mathbf{z}^h \in \mathbf{V}^h$ is an approximation of $\mathbf{z}$ which is considered here as point interpolation of the dual solution, $\mathbf{z}^h = I^h\mathbf{z}$. Splitting the global integration over Ω into subdomains accounting for the contribution of the elements $K \in \mathbb{T}^h$ and integrating by parts element-wise yields

$$J(\mathbf{e}) \;=\; \sum_{K\in\mathbb{T}^h} \left\{ \left(-\nabla\cdot[\mathbb{C} : \boldsymbol{\varepsilon}(\mathbf{e})], \mathbf{e}^Q\right)_K + \left(\mathbf{n}\cdot[\mathbb{C} : \boldsymbol{\varepsilon}(\mathbf{e})], \mathbf{e}^Q\right)_{\partial K} \right\} \tag{4.6}$$

Knowing that $-\nabla\cdot[\mathbb{C} : \boldsymbol{\varepsilon}(\mathbf{u})] = f$ and with the traction continuity of $\mathbf{n}\cdot[\mathbb{C} : \boldsymbol{\varepsilon}(\mathbf{u})]$ across inter element edges, the error is represented as

$$J(\mathbf{e}) \;=\; \sum_{K\in\mathbb{T}^h} \left\{ \left(\mathbf{R}^h, \mathbf{e}^Q\right)_K + \left(\mathbf{r}^h, \mathbf{e}^Q\right)_{\partial K} \right\} \tag{4.7}$$

where K and ∂K denote an element and its boundary, respectively. The edge residual $\mathbf{r}^h$ and element residual $\mathbf{R}^h$ are given in Eqs. (3.6) and (3.5), respectively.

4.2.2 Elastoplasticity problem

Considering that in the variational form of elastoplastic problem (Eq. (2.27)) the semi-linear form $a(\cdot)(\cdot)$ is not differentiable, the formal approach developed for the elasticity problem [24, 30] explained in Sec. 4.2.1 cannot be used directly. However, we can apply it heuristically for deriving weighted a posteriori error estimators in the FEM approximation [17]. Afterwards, it needs to be verified by numerical investigations. Its success can be explained by theoretical justification that the non-differentiability of the function $\mathbb{C}$ occurs solely in the elastic-plastic transition zone which is expected to be lower-dimensional [17]. Consider the following approximate dual problem

$$\Big(\mathbb{C}^{lin}(\boldsymbol{\varepsilon}(\mathbf{u}^h)) : \boldsymbol{\varepsilon}(\mathbf{v}), \boldsymbol{\varepsilon}(\mathbf{z})\Big) = J(\mathbf{v})\,, \qquad \forall \mathbf{v} \in \mathbf{V}_0\,. \tag{4.8}$$

where $\mathbb{C}^{lin}(\cdot)$ is defined in Eq. (2.32). It is noted that the dual problem is formed based on the converged solution of the primal problem and is linear. The following error in the QoI can be obtained by applying the formal procedure of the DWR error estimation in the elasticity problem [17] and disretizing the domain into meshes $\mathbb{T}^h$.

$$J(\mathbf{e}) = \sum_{K \in \mathbb{T}^h} \left\{ \Big(\mathbf{R}^h, \mathbf{z} - \mathbf{z}^h\Big)_K + \Big(\mathbf{r}^h, \mathbf{z} - \mathbf{z}^h\Big)_{\partial K} \right\} + \mathbf{R}^{h(2)}\,, \qquad \mathbf{z}^h \in \mathbf{V}^h\,. \tag{4.9}$$

where K and ∂K denote an element and its boundary, respectively. The remainder term $R^{h(2)}$ is quadratic in the error $\mathbf{e}$ in regions where the function $\mathbb{C}$ is twice differentiable. The elasto-plastic transition zone is the questionable region, since regularity fails. This term is neglected. The edge and element residuals in Eq. (4.9) are according to the Eqs. (3.6) and (3.5), respectively.

The edge residual, $\mathbf{r}^h|_\Gamma$, is obtained by exchanging half of the edge integral of the element K with its neighbor element K' and considering the opposite sign of their normal vectors.

The final form of (4.9) can be obtained by setting the discrete function $\mathbf{z}^h$, which is arbitrary, to the point interpolation of the dual solution, $\mathbf{z}^h = I^h\mathbf{z}$,

$$J(\mathbf{e}) = \sum_{K \in \mathbb{T}^h} \left\{ \Big(\mathbf{R}^h, \mathbf{z} - I^h\mathbf{z}\Big)_K + \Big(\mathbf{r}^h, \mathbf{z} - I^h\mathbf{z}\Big)_{\partial K} \right\}. \tag{4.10}$$

Eq. (4.10) represents the error of the finite element discretization with respect to the functional $J(\cdot)$. The Dual Weighted Residual (DWR) is a weighted form of the residual error estimator, where $\mathbf{z} - I^h\mathbf{z}$ are weights indicating the importance of the element-wise residuals for the evaluation of the given functional. Since it is an element-wise quantity, it can be applied as a mesh adaptation criterion. However, the DWR requires

the dual solution $\mathbf{z}$, which conveys the information about the quantity of interest. For this purpose, we compute the dual solution numerically, and approximate $\mathbf{z}$ by some numerically obtained $\tilde{\mathbf{z}}$. It is noted that we cannot apply the same method as used for solving the primal solution $\mathbf{u}^h$, otherwise $\mathbf{z} - I^h\mathbf{z} = 0$, and the overall error estimate would be zero. Rather, the approximation $\tilde{\mathbf{z}}$ has to be from a larger space than the primal finite element space. There are various ways to obtain such an approximation. In this contribution, we compute it in one higher order finite element space.

4.3 Quantity of interest functional

The dual problem, Eq. (4.8), is defined by a functional corresponding to the quantity of interest. In this contribution three quantities including the point displacement and average value of stress on a specific surface and in a region are of interest. If the QoI functional is non-linear, it can be linearized and then be used [21, 44]. Such a treatment is performed where average stress over a region is of interest.

4.3.1 Displacement at a point

Firstly, consider the displacement $\mathbf{u}(\mathbf{x}_0)$ at a point $\mathbf{x}_0$ as the quantity of interest. By using the definition of the Dirac delta function, δ, the corresponding functional is defined as

$$J(\mathbf{v}) = \mathbf{v}(\mathbf{x}_0) = \int_\Omega \mathbf{v}\delta(\mathbf{x} - \mathbf{x}_0)d\Omega\,. \tag{4.11}$$

4.3.2 Average stress on a surface

As a second quantity of interest, consider the mean value of a stress component $\sigma_{ij}^{av}|_S\,(i,j = x,y\,(,z))$ on a specified edge S in 2d or area S in 3d. The quantity of interest functional can be written as

$$J(\mathbf{v}) = \frac{1}{|\Gamma_S|}\int_{\Gamma_S} \sigma_{ij}(\mathbf{v}) d\Gamma, \qquad i,j = x,y,z\,. \tag{4.12}$$

where $|\Gamma_S|$ is the length of the edge S in 2d or the area of the surface S in 3d. Although, this QoI is a nonlinear functional for the elastoplastic problem, we do not linearize it since it is computed on the (element) boundary and its linearized form needs 2^{nd} derivative of the solution and we would rather apply linearization where an (element) domain is considered and a dual problem of 2^{nd} order or higher is defined.

4.3.3 Average stress in a region

The other quantity of interest which is investigated in this study is the mean value of a stress component $\sigma_{ij}^{av}|_{\Omega_0}\,(i,j = x,y,z)$ in a region Ω_0. Consequently, the following functional is introduced

$$J(\mathbf{v}) = \frac{1}{|\Omega_0|}\int_{\Omega_0} \sigma_{ij}(\mathbf{v}) d\Omega, \qquad i,j = x,y,z\,, \tag{4.13}$$

where $|\Omega_0|$ is the volume of the region Ω_0 in the 3d case. Since the stress is a nonlinear function of displacement $\mathbf{u}$, Eq. (4.13) is a nonlinear functional.

In such a case, we need to firstly linearize the functional to apply the goal-oriented error estimation methodology. For this purpose, we utilize the Taylor expansion,

$$\begin{aligned} J(\mathbf{u}) &= J(\mathbf{u}^h) + \nabla J(\mathbf{u}^h)\cdot(\mathbf{u}-\mathbf{u}^h) + \cdots \\ &= J(\mathbf{u}^h) + \nabla J(\mathbf{u}^h)\cdot\mathbf{e} + \cdots\,, \end{aligned} \tag{4.14}$$

$$J(\mathbf{u}) - J(\mathbf{u}^h) \cong \nabla J(\mathbf{u}^h)\cdot\mathbf{e}\,, \tag{4.15}$$

$$J^{lin}(\mathbf{e}) = \nabla J(\mathbf{u}^h) \cdot \mathbf{e}\,. \tag{4.16}$$

Subsequently, we can apply the aforementioned goal-oriented error estimation by replacing the QoI functional $J(\mathbf{v})$ in the dual problem, Eq. (4.2) for elasticity problem and Eq. (4.8) for elastoplasticity problem, with the linearized QoI functional

$$J^{lin}(\mathbf{v}) = \nabla J(\mathbf{u}^h) \cdot \mathbf{v}\,. \tag{4.17}$$

where it is defined according to the approximated solution of the primal problem $\mathbf{u}^h$. Correspondingly, the QoI functional (4.13) is linearized as follows

$$J^{lin}(\mathbf{v}) \;=\; \frac{1}{|\Omega_0|}\int_{\Omega_0} \nabla\sigma_{ij}(\mathbf{u}^h) \cdot \mathbf{v} d\Omega, \qquad i,j = x,y,z\,. \tag{4.18}$$

Chapter 5

Mesh adaptivity

In the FEM, mesh discretization highly affects the solution accuracy and obviously the computational effort. Since simulation of complicated problems, especially nonlinear ones in three dimensions are computationally expensive, it is of great importance to be able to minimize the computational effort while the expected solution accuracy is gained.

Adaptivity methods are the keys to achieve this goal. Adaptive methods can be categorized into three different classes: h-, r- and p-adaptivity. In h-adaptivity the discretization is refined while p-adaptivity refers to locally increasing the polynomial order of the shape functions. R-adaptivity aims to find the optimal mesh topology for a given discretization. P-adaptivity is not well suited for problems involving localized deformation and plasticity since high gradients and localized deformation cannot be captured well with higher order. In this contribution, we consider h-adaptivity where the mesh is refined and coarsened based on the estimated element-wise errors.

5.1 Adaptivity criterion

Different criteria can be adopted in the mesh adaptivity procedure. In this work, global refinement indicator is computed based on the element-wise errors. For example in the

goal-oriented error estimation, the local refinement indicators are computed according to Eq. (4.10),

$$\eta_K = \left\| \left(\mathbf{R}^h, \mathbf{z} - I^h \mathbf{z} \right)_K + \left(\mathbf{r}^h, \mathbf{z} - I^h \mathbf{z} \right)_{\partial K} \right\|_{L_2} \qquad K \in \mathbb{T}^h \,, \tag{5.1}$$

which are used to steer the mesh adaptation. Subsequently, the global refinement indicator is derived as

$$\eta = \left(\sum_{K \in \mathbb{T}^h} \eta_K^2 \right)^{1/2} . \tag{5.2}$$

By specifying a permissible value $\eta_{\max}$, the mesh adaptivity is automatically performed whenever $\eta > \eta_{\max}$.

5.2 Mesh Adaptivity

Mesh adaptation can be categorized into two classes: (a) Remeshing and (b) Local refinement. Fig. 5.1 demonstrates these techniques schematically. In the remeshing process mesh configuration in the whole domain is reconstructed while in the local refinement, a range of elements are locally refined.

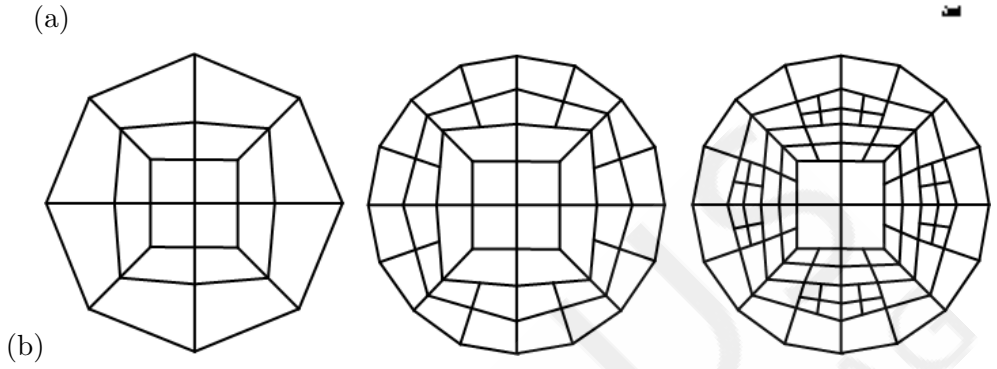

FIGURE 5.1: Mesh adaptivity strategies: (a) Remeshing, (b) Local refinement.

In order to perform a continuous analysis, solution variables need to be transferred from the previous mesh to the new mesh after each mesh adaptation. In the remeshing case, this process introduce more errors. Therefore, in this work hierarchical mesh refinement and also coarsening is performed in order to increase the efficiency.

The applied mesh adaptivity procedure is demonstrated in Fig. 5.2.

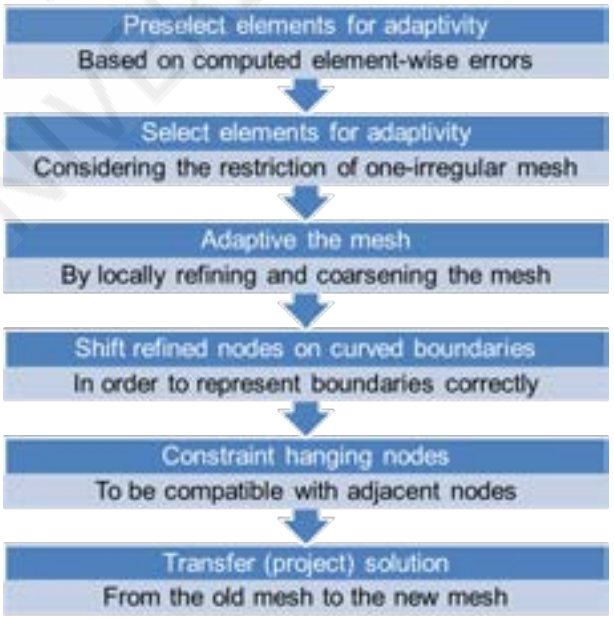

FIGURE 5.2: Mesh adaptivity procedure by using local refinement.

Mesh adaptation is carried out with the knowledge of element-wise errors/refinement indicators. Calculated errors are firstly sorted. The 30 percent of the elements with the highest errors are selected to be refined and the 3 percent of those with the lowest errors are chosen to be coarsened. Based on an algorithm restriction, each face of an element is divided at most once. Therefore, some additional elements are required to be refined. Afterwards, the selected elements are refined by defining new nodes at the middle of each element edge (and element face in 3d case). Therefore, the mesh structure remains simple.

In the case of curved boundaries, the new inserted nodes should be moved to its projected point on the boundary. Fig. 5.3 demonstrates the refinement procedure along a curved boundary in 2d.

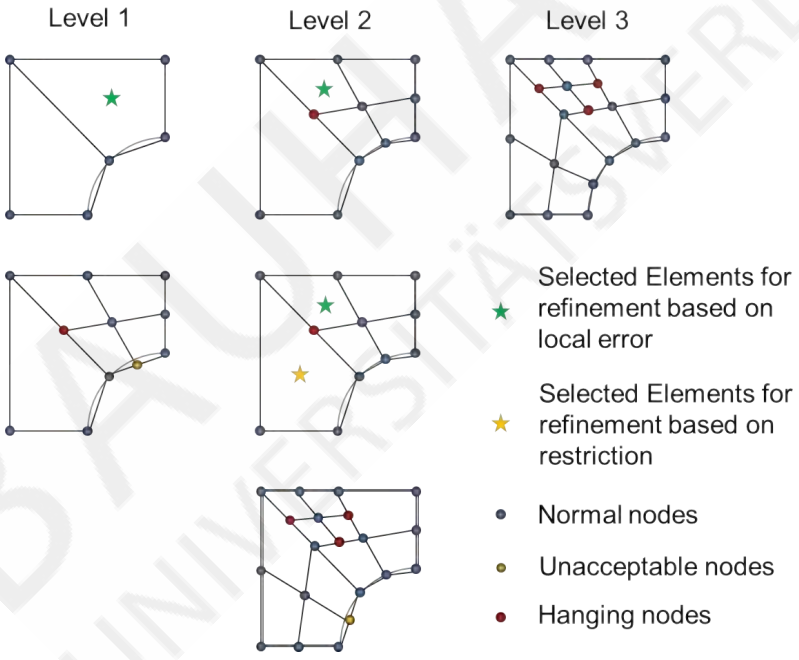

FIGURE 5.3: Two mesh adaptivity steps by using local refinement.

Since, quadrilateral and hexahedral elements are applied in this work, refinement introduces hanging nodes. The hanging nodes should be constrained to be compatible with adjacent nodes, so that the function has no jump at the boundary of small and large elements. Fig. 5.4 illustrates the hanging nodes in refined quadrilateral and hexahedral elements and their corresponding constraint formulations. The hanging nodes are

not counted as unknown degrees of freedom. They are utilized to modify the global stiffness matrix. After solving the algebraic equations, the hanging nodes' solutions are calculated based on the solution of unknown degrees of freedom and the constraints demonstrated in Fig. 5.4.

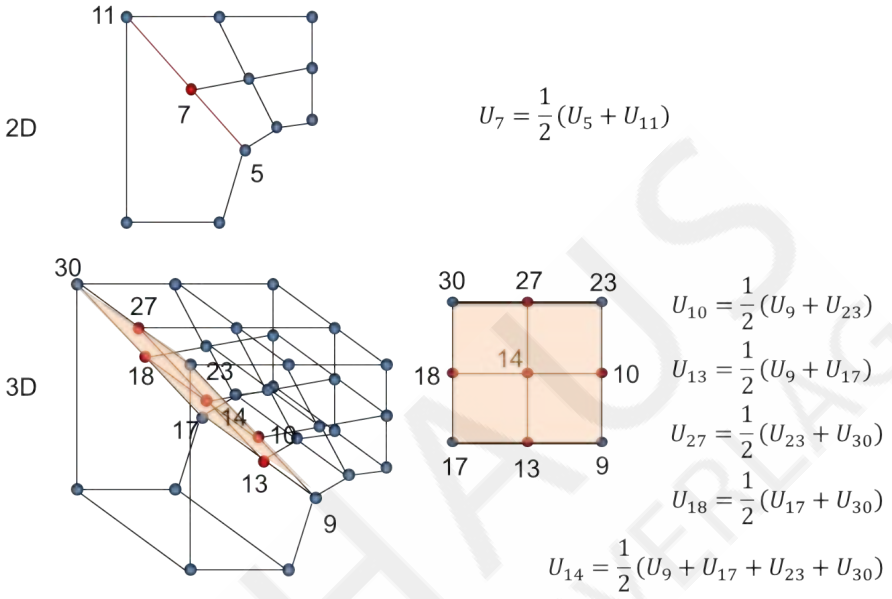

FIGURE 5.4: Hanging nodes introduced by refining the quarilateral and hexahedral elements and their corresponding constraints.

The nodal solutions and solution variables at Gauss points are transferred and projected to the new mesh after each mesh adaptivity procedure.

5.3 General Algorithm

In the following, schematic algorithms for goal-oriented mesh adaptivity in elasticity and elastoplasticity problems are demonstrated.

5.3.1 Goal-oriented mesh adaptivity in elasticity problems

Fig. 5.5 illustrates the schematic algorithm for goal-oriented mesh adaptivity in elasticity problems. Firstly, the primal problem is solved. Afterwards, by solving the dual problem, error in QoI and consequently the global refinement indicator, η, (Eq. (5.2)) is calculated

and it is compared with the prescribed permissible value $\eta_{\max}$ and if $\eta > \eta_{\max}$, mesh adaptivity is performed and the same procedure is repeated until $\eta \leq \eta_{\max}$.

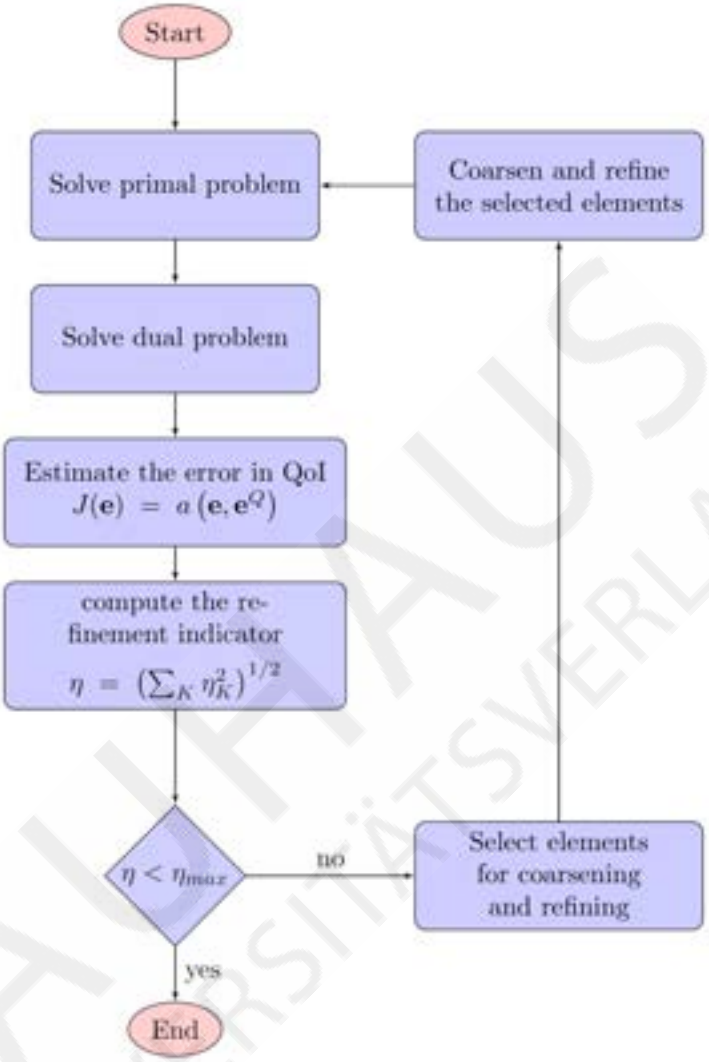

FIGURE 5.5: Genral algorithm for goal-oriented mesh adaptivity in elasticity problem.

5.3.2 Mesh adaptivity in elastoplasticity problems

In the elastoplasticity case, error estimation is carried out at the end of each load/displacement increment after convergence satisfaction of the iteration process. If the global refinement indicator (calculated according to the element-wise errors) is higher than the prescribed permissible value, mesh adaptation is performed and the solution variables are projected into the new mesh. Except for the first load/displacement increment, mesh adaptation is allowed only once. The whole schematic procedure is depicted in Fig. 5.6.

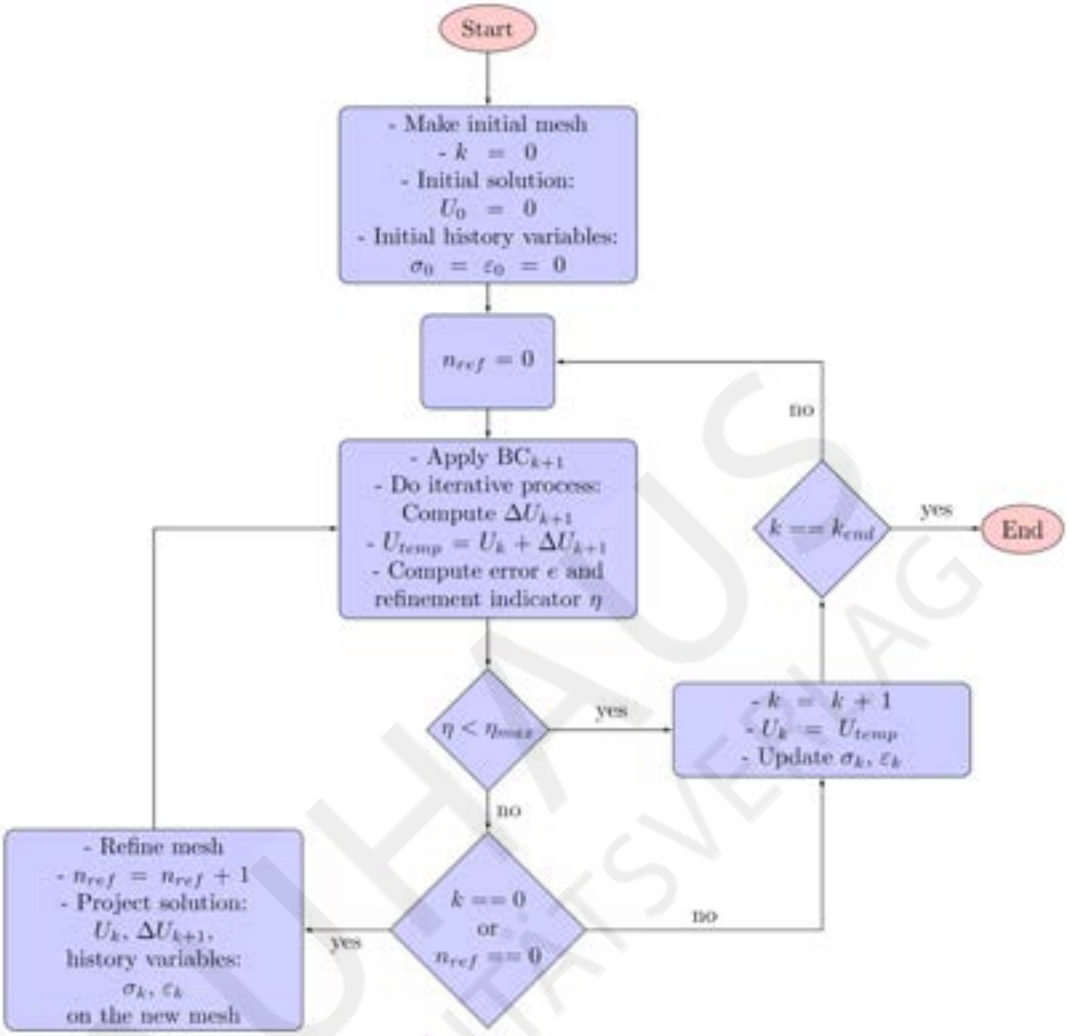

FIGURE 5.6: Genral algorithm for error estimation and mesh adaptivity in elastoplasticity problem.

Chapter 6

Numerical Examples

In spite of the goal-oriented mesh adaptivity process, mesh adaptivity based on global refinement and conventional recovery- and residual-based error estimations are also performed to be able to compare the results. In the global refinement process, all elements are subdivided by 4 and 8 elements at each refinement step in 2d and 3d, respectively. In order to do h-adaptivity, a recovery-based error estimation developed by Kelly et al. [28] and the residual-based error estimation (see Chapter 3) and goal-oriented error estimation scheme (see Chapter 4) have been applied. The elements are sorted according to the error magnitude. The elements which belong to the 30% of the elements with higher errors are selected for refinement and the elements which are within the 3% of the elements with lowest errors are coarsened in the next adaptive step, i.e. 4 and 8 refined elements are replaced by a 4- and 8-times bigger element in 2d and 3d, respectively. It is noted that coarsening only occurs if all the refined elements (children) belonging to a bigger element in one higher refinement level (mother) are selected to be coarsened.

6.1 Linear Elasticity Problems

6.1.1 Plate with a hole under far-field uni-directional tension [29]

In order to verify the proposed approach and compare it with other introduced techniques, we consider firstly a plate with a centered circular hole of radius a subjected to far-field uni-directional tension, σ_∞, along the x-direction (see Fig. 6.1). The analytical solution of stress is given by,

$$\begin{aligned}
\sigma_{xx}(r,\theta) &= \sigma_\infty \left[1 - \frac{a^2}{r^2}\left(\frac{3}{2}\cos 2\theta + \cos 4\theta\right) + \frac{3}{2}\frac{a^4}{r^4}\cos 4\theta\right] \\
\sigma_{yy}(r,\theta) &= \sigma_\infty \left[-\frac{a^2}{r^2}\left(\frac{1}{2}\cos 2\theta - \cos 4\theta\right) - \frac{3}{2}\frac{a^4}{r^4}\cos 4\theta\right] \\
\sigma_{xy}(r,\theta) &= \sigma_\infty \left[-\frac{a^2}{r^2}\left(\frac{1}{2}\sin 2\theta + \sin 4\theta\right) + \frac{3}{2}\frac{a^4}{r^4}\sin 4\theta\right]
\end{aligned} \tag{6.1}$$

where r and θ are the usual polar coordinates centered at the center of the hole.

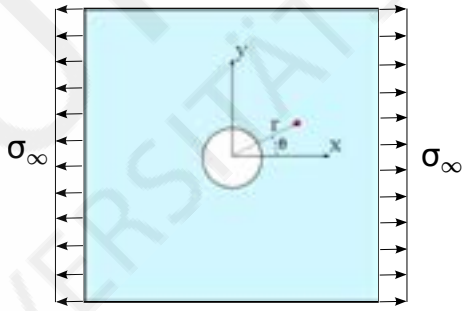

FIGURE 6.1: The plate with hole subjected to far-field uni-directional tension.

Regarding the problem symmetry, just a quarter of the plate with finite dimensions, as illustrated in Fig. 6.2, is modeled where the top and right edges are subjected to the tractions obtained from analytical stresses, as follow

$$\bar{\mathbf{t}} = \boldsymbol{\sigma} \cdot \mathbf{n} \tag{6.2}$$

where $\boldsymbol{\sigma}$ is the stress tensor and $\mathbf{n}$ is the unit vector normal to the corresponding surface.

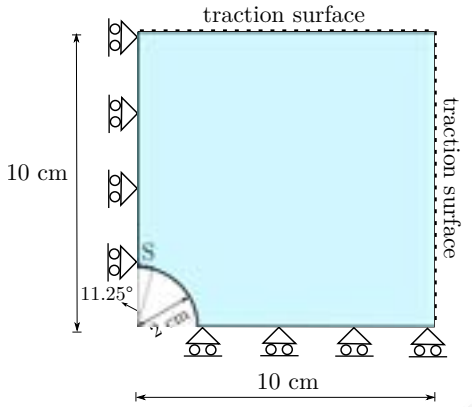

FIGURE 6.2: Geometry and boundary conditions of the plate with hole subjected to tension.

The following parameters are considered for modeling the problem with steel material:

Far-field stress $\sigma_\infty = 100$ MPa, Young's modulus $E = 200$ GPa and Poisson's ratio $\nu = 0.3$.

The average value of stress σ_{xx} on the surface S which is 1/8 of the curved surface (see Fig. 6.2), $\sigma^{av}_{xx}|_S$, is considered as the quantity of interest. The analytical solution is $\sigma^{av}_{xx}|_S = 291.19$ MPa.

Firstly, 32 elements are used for discretization (see Fig. 6.3). Different strategies including global refinement and adaptivity based on estimated errors by using Kelly, residual and goal-oriented error estimation have been applied and investigated. Each methodology leads to different element errors and therefore, the resulting meshes are different. Fig. 6.4 illustrates the resulting meshes at the 4-th adaptivity step of different schemes. It is seen that in the goal-oriented adaptivity mesh concentration is around the surface S where the quantity of interest has been defined.

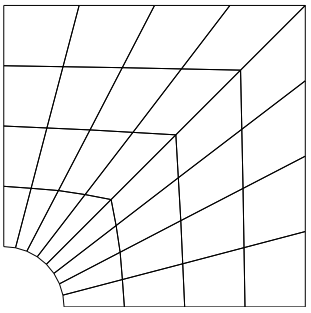

FIGURE 6.3: Initial descritization of the plate with hole subjected to tension.

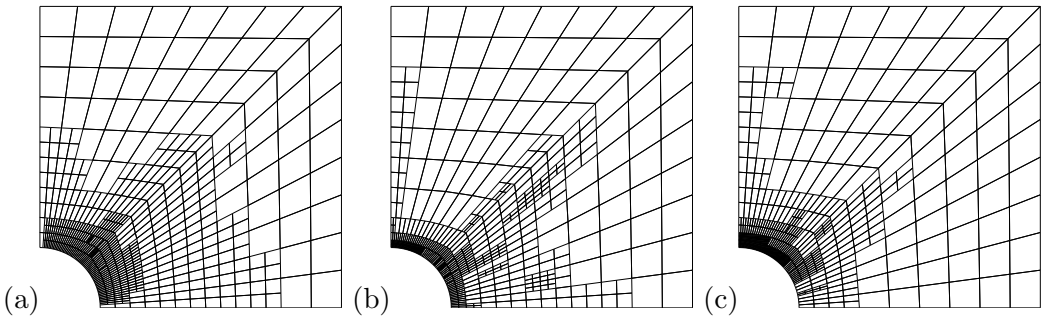

FIGURE 6.4: Meshes at the 4-th adaptivity step of the plate with hole subjected to tension by applying: (a) Kelly refinement, (b) residual-based adaptivity and (c) DWR adaptivity.

The relative errors of the $\sigma_{xx}^{av}|_S$ are depicted in Fig. 6.5. It is seen that the goal-oriented error estimation leads to an adaptivity process with much better convergence rate.

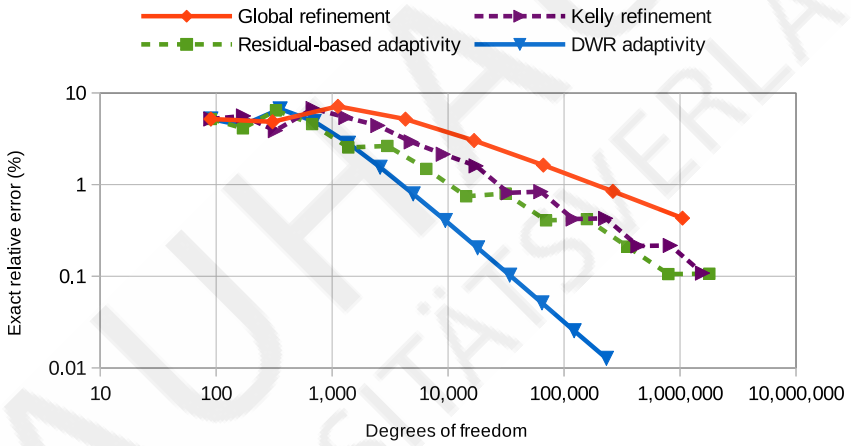

FIGURE 6.5: Exact relative errors (%) of $\sigma_{xx}^{av}|_S$ versus degrees of freedom for the plate with hole subjected to tension.

Since for applying the GOEE, an auxiliary/dual problem needs to be solved, for the same degrees of freedom, more computational effort is required especially that for the current case dual problem is solved by adopting one higher order finite elements. In order to evaluate the efficiency of the proposed goal-oriented adaptivity process, Fig. 6.6 depicts the exact relative error (%) of $\sigma_{xx}^{av}|_S$ versus the consumed computational time (sec). It is shown that for achieving very precise solution, the goal-oriented adaptivity is the most efficient method.

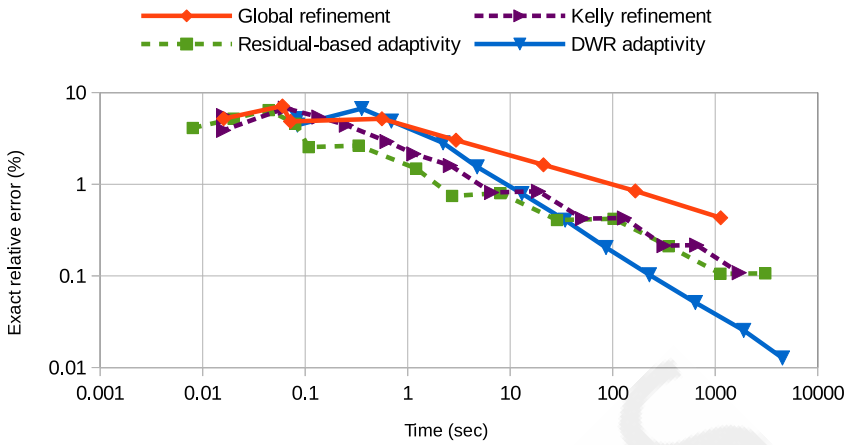

FIGURE 6.6: Exact relative errors (%) of $\sigma_{xx}^{av}|_S$ versus computational times (sec) for the plate with hole subjected to tension.

6.1.2 Point displacement evaluation of a square-shape sample under pressure and shear [29]

Consider a plane strain problem with the loading and boundary conditions shown in Fig. 6.7 and the average material properties of clay:

Modulus of elasticity $E^{av} = 30$ MPa, Poisson's ratio $\nu^{av} = 0.2$.

It is assumed that the material remains elastic under the imposed loading. The uniform distributed 21×21 nodes are considered as the initial discretization. Displacement at the Point A is the quantity of interest.

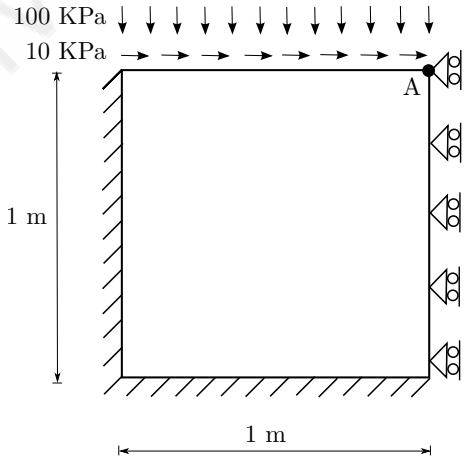

FIGURE 6.7: Geometry and boundary conditions of the square-shape problem.

In the following, the goal-oriented mesh adaptivity procedure is applied to homogeneous, 2-materials layered and heterogeneous cases to investigate the effect of material change and heterogeneity on the mesh adaptivity process and the resulted meshes.

Since the analytical solutions are not available, the quantity of interest value calculated in the finest mesh obtained in the goal-oriented mesh adaptivity (by using GOEE) is considered as the reference solution and is applied for estimating the error of other simulations.

6.1.2.1 Homogeneous case

Firstly, the material is assumed homogeneous. Displacement at the Point A in the finest mesh obtained in the goal-oriented mesh adaptivity with 532,572 DoFs is considered as the reference solution ($\mathbf{u}_A = 2.99199$ mm) and is applied for estimating the error of quantity of interest in other simulations.

Fig. 6.8 shows the first six mesh configurations obtained in the Goal-oriented adaptive process. Fig. 6.9 demonstrates the mesh configuration at the 4-th adaptivity step of different strategies. It is seen that the meshes resulted by the estimated errors are so different. The GOEE-based adaptivity leads to more mesh concentration around the Point A whose displacement is of interest.

Relative errors (in percentage) of Point A displacement for global refinement and different mesh adaptivity strategies are illustrated in Fig. 6.10. Superiority of the Goal-oriented mesh adaptivity is shown compared to the other conventional mesh-adaptivity schemes.

6.1.2.2 2-materials layered case

In this section, for better demonstrating the effect of material change on the mesh-adaptivity procedure, the two-material layered as shown in Fig. 6.11 is investigated.

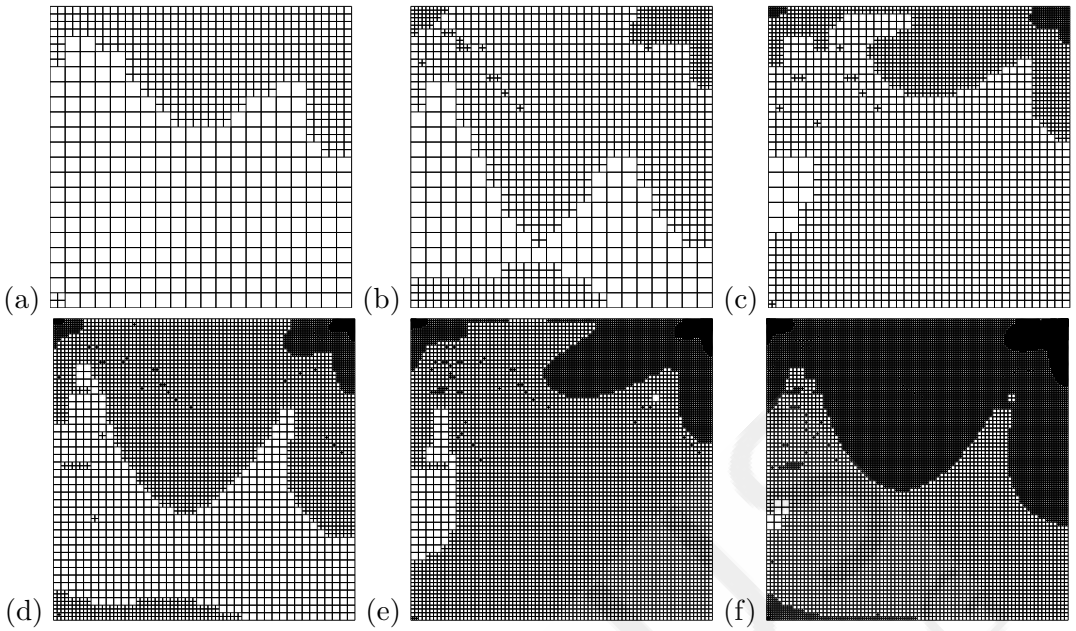

FIGURE 6.8: DWR-based mesh adaptivity of the square-shape sample under pressure and shear in homogeneous case: (a) Step 1 with 1694 DoFs, (b)Step 2 with 3,274 DoFs, (c) Step 3 with 6,162 DoFs, (d) Step 4 with 11,712 DoFs, (e) Step 5 with 21,984 DoFs, (f) Step 6 with 41,606 DoFs.

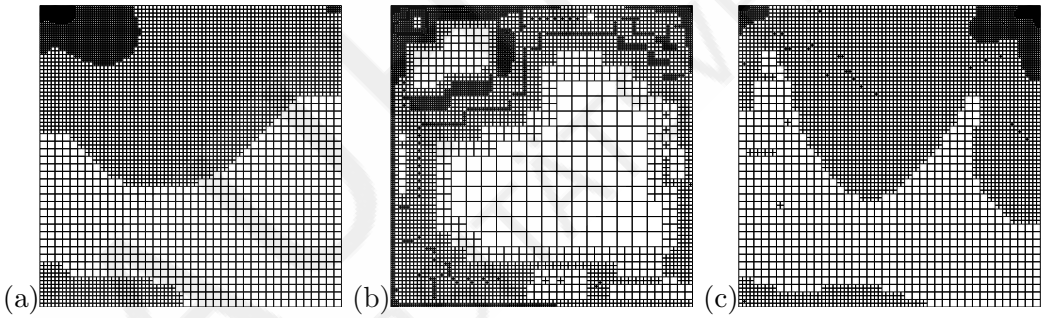

FIGURE 6.9: Meshes at the 4-th adaptivity step of the square-shape sample under pressure and shear in homogeneous case by applying: (a) Kelly refinement, (b) residual-based adaptivity and (c) goal-oriented adaptivity.

Mesh configurations of the first six adaptive steps obtained by applying DWR error estimation are shown in Fig. 6.12 and Fig. 6.13 depicts the resulted meshes of 4-th adaptivity step of different strategies. It is seen that dense elements are formed along the material change line and the adaptivity procedures capture it well. Among the applied methodologies, goal-oriented adaptivity results in mesh concentration around the Point A, too.

The reference $\mathbf{u}_A = 3.47691$ mm is taken from the finest solution of the GOEE-based adaptivity with 414,656 degrees of freedom. The relative errors are plotted in Fig. 6.14.

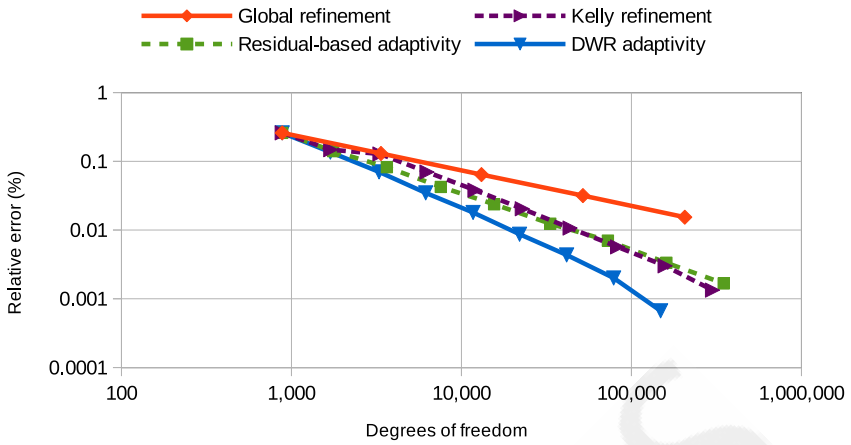

FIGURE 6.10: Relative errors (%) of $\mathbf{u}_A$ in homogeneous case.

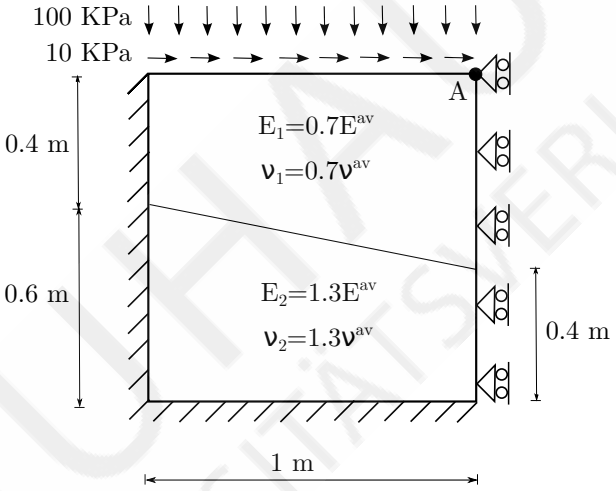

FIGURE 6.11: Geometry and boundary conditions of the 2-material layered problem.

6.1.2.3 Heterogeneous case

In this section, a heterogeneous material is considered. The material heterogeneity is modeled by producing a random field consisting of 101×101 uniformly distributed points by the correlation variables 0.95 and 0.01 in x and y directions, respectively and scaling them to [0.7, 1.3] (see Appendix A). Random variable inside the intervals (squares) are obtained by averaging the random variables at the square vertices. Therefore, at each arbitrary point, a random value is defined. The resulting random field is shown in Fig. 6.15. The material properties, E^{av} and ν^{av}, are multiplied by this random field.

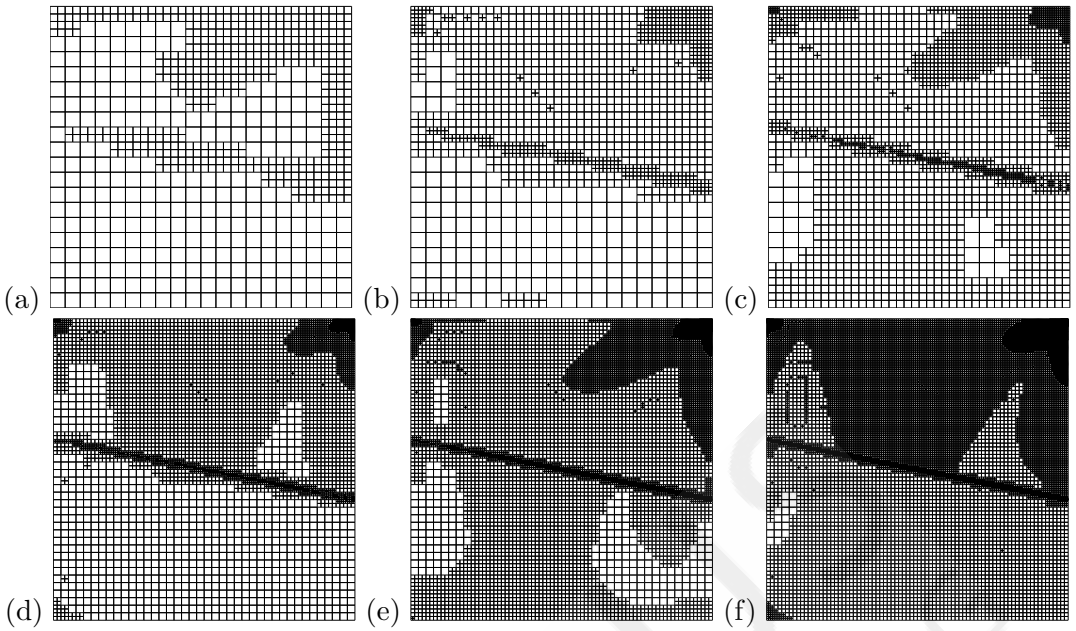

FIGURE 6.12: GOEE-based mesh adaptivity of the square-shape sample under pressure and shear in 2-material layered case: (a) Step 1 with 1,742 DoFs, (b)Step 2 with 3,444 DoFs, (c) Step 3 with 6,916 DoFs, (d) Step 4 with 13,642 DoFs, (e) Step 5 with 27,204 DoFs, (f) Step 6 with 53,592 DoFs.

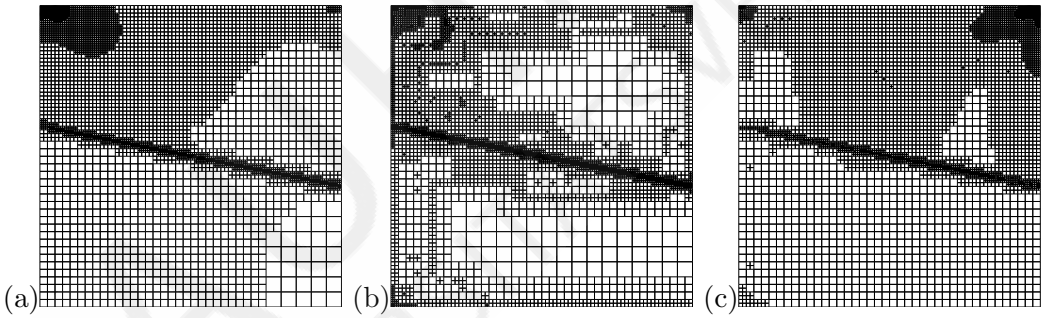

FIGURE 6.13: Meshes at the 4-th adaptivity step of the square-shape sample under pressure and shear in 2-material layered case by applying: (a) Kelly refinement, (b) residual-based adaptivity and (c) DWR adaptivity.

The reference $\mathbf{u}_A = 3.16901$ mm is taken from the fine mesh, with 681,284 DoFs, obtained in the 10-th adaptivity step by using the GOEE. Mesh configurations of different GOEE-based adaptivity steps are illustrated in Fig. 6.16. Fig. 6.17 presents the resulted meshes in the 4-th adaptivity step of the applied methodologies. It is seen that mesh obtained from the residual-based adaptivity captures the highly material changes more in comparison with the goal-oriented adaptivity. Because the local effect of the elements around the point A on the error of the QoI is dominant in this problem.

The resulting relative errors are depicted in Fig. 6.18. It shows the superiority of

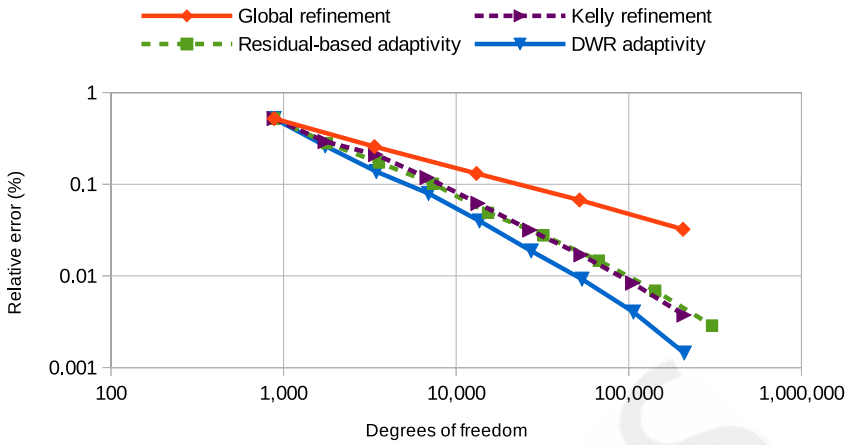

FIGURE 6.14: Relative errors (%) of $\mathbf{u}_A$ in 2-material layered case.

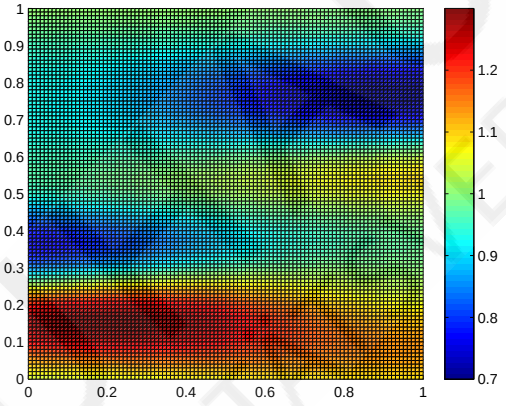

FIGURE 6.15: Random field in the range [0.7,1.3] for the square-shape problem.

the proposed adaptivity approach over other conventional approaches when a specific quantity is of interest.

6.1.3 Mean stress evaluation on a surface in a square-shape sample with a hole under pressure [29]

Consider a plane strain problem with the geometry and boundary conditions shown in Fig. 6.19 made out of concrete with the following material properties.

Modulus of elasticity $E^{av} = 14$ GPa, Poisson's ratio $\nu^{av} = 0.15$, pressure $P = 3$ MPa and density $\rho = 2400$ kg/m^3.

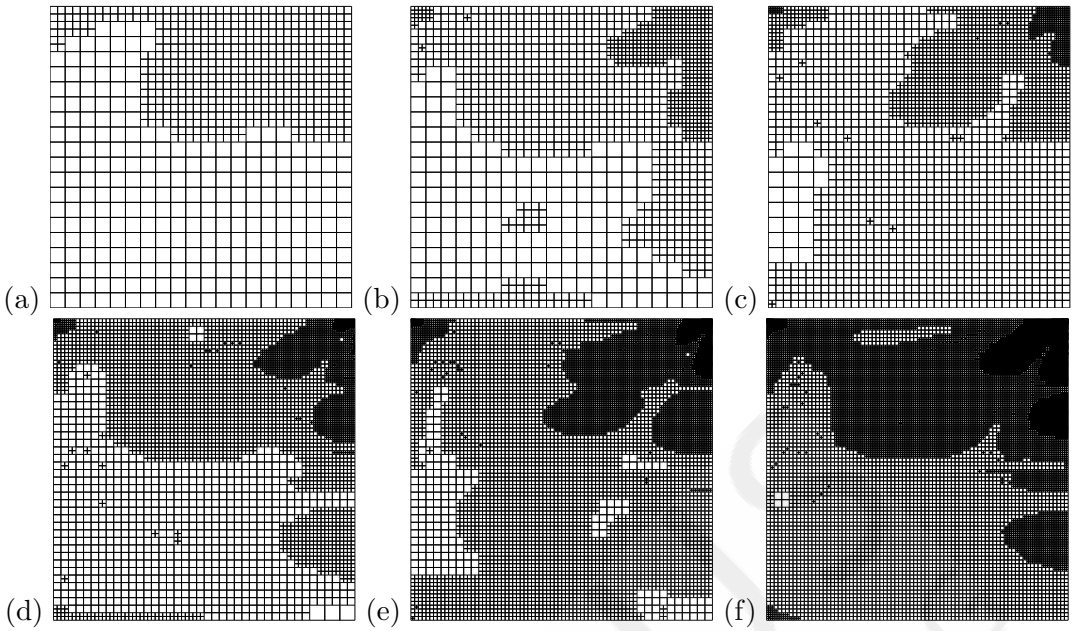

FIGURE 6.16: GOEE-based mesh adaptivity of the square-shape sample under pressure and shear in heterogeneous case: (a) Step 1 with 1722 DoFs, (b)Step 2 with 3,374 DoFs, (c) Step 3 with 6,472 DoFs, (d) Step 4 with 12,488 DoFs, (e) Step 5 with 23,766 DoFs, (f) Step 6 with 45,612 DoFs.

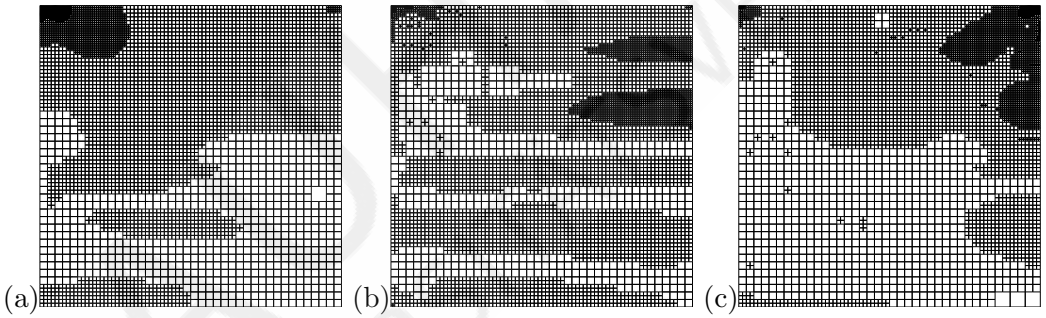

FIGURE 6.17: Meshes at the 4-th adaptivity step of the square-shape sample under pressure and shear in heterogeneous case by applying: (a) Kelly refinement, (b) residual-based adaptivity and (c) DWR adaptivity.

The material remains in linear elastic state under the imposed loading. The average stress on the curved surface S, $\sigma^{av}_{yy}|_S$, is of interest. Fig. 6.20 illustrates the initial discretization.

Like the previous example, Section 6.1.2, the goal-oriented mesh adaptivity is performed for both homogeneous and heterogeneous material to study the heterogeneity effect on the refined meshes.

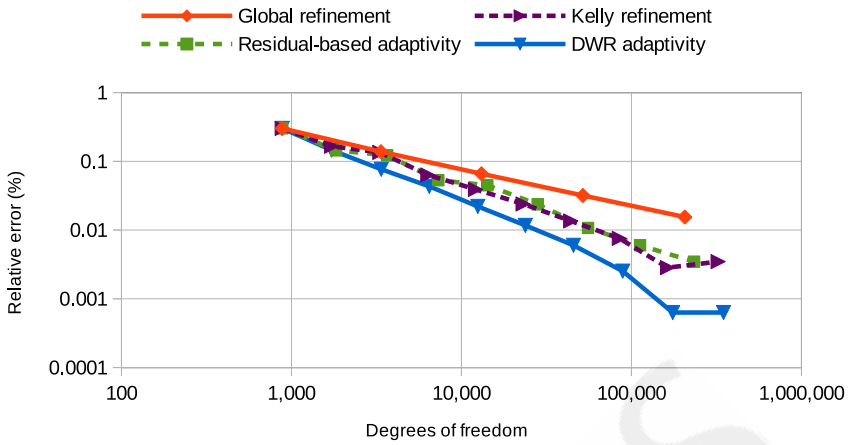

FIGURE 6.18: Relative errors (%) of $\mathbf{u}_A$ in heterogeneous case.

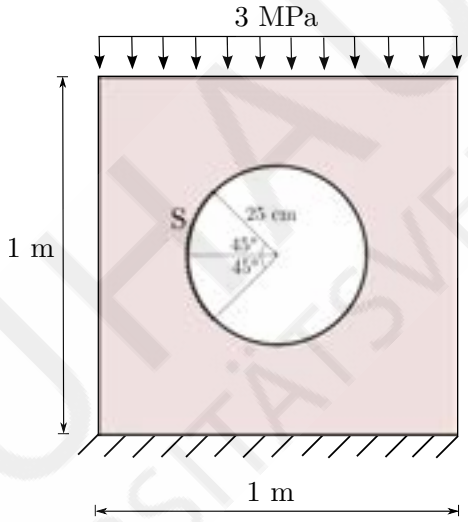

FIGURE 6.19: Geometry and boundary conditions of concrete under pressure.

6.1.3.1 Homogeneous case

Firstly, the concrete material is assumed homogeneous. The average stress on the curved face S, $\sigma_{yy}^{av}|_S = -8,730,730$ Pa, at the finest mesh (with 232,038 degrees of freedom) obtained by goal-oriented adaptivity is considered as reference solution and is used for approximating the error of $\sigma_{yy}^{av}|_S$ in other simulations. Discretization of the first six adaptivity steps applied in the goal-oriented adaptivtiy are shown in Fig. 6.21. It is seen that mesh concentration is more around the surface S.

The resulting relative error (in percentage) of $\sigma_{yy}^{av}|_S$ for all the simulations are plotted in Fig. 6.22. The average convergence rate of global refinement and mesh adaptivities

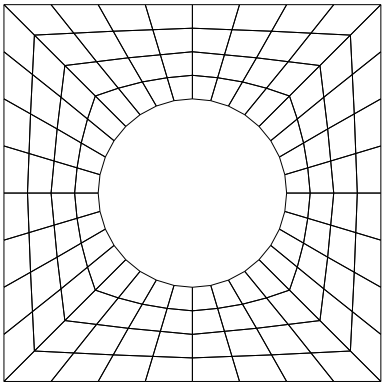

FIGURE 6.20: Initial mesh considered for the problem of concrete under pressure.

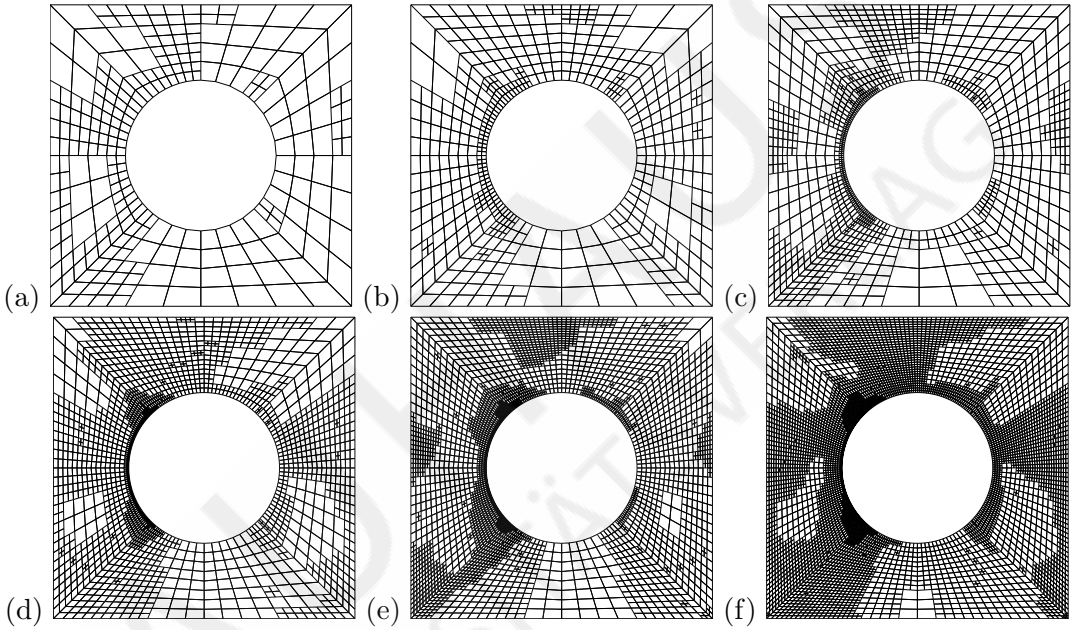

FIGURE 6.21: GOEE-based mesh configuration based adaptivity of the sample with a hole under pressure in homogeneous case: (a) Step 1 with 654 DoFs, (b)Step 2 with 1,312 DoFs, (c) Step 3 with 2,556 DoFs, (d) Step 4 with 4,854 DoFs, (e) Step 5 with 9,390 DoFs, (f) Step 6 with 17,758 DoFs.

based on Kelly-, residual-based and goal-oriented error estimations are 0.36, 0.40, 0.50 and 1.05, respectively. It is shown that the convergence rate of goal-oriented adaptivity is much higher than other applied methods.

6.1.3.2 Heterogeneous case

Since the concrete is not fully homogeneous, its heterogeneity is assumed by two random fields in the range [0.7,1.3] (see Fig. 6.23) which is multiplied by E^{av} and ν^{av} considered

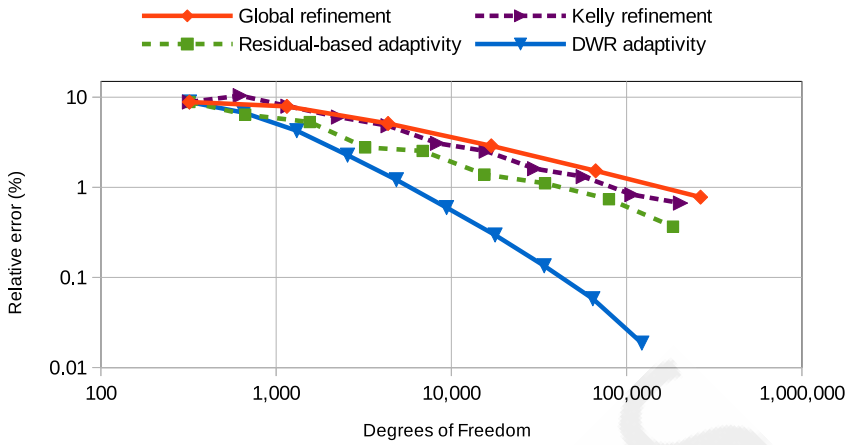

FIGURE 6.22: Relative errors (%) of $\sigma_{yy}^{av}|_S$ in homogeneous concrete under pressure.

in the homogeneous case. The random fields are produced by applying uniformly distributed points with the horizontal and vertical $\frac{1}{110}$ m distances by applying the Gauss correlation variables [0.03, 0.01] and [0.05, 0.04], respectively (see Appendix A). At each arbitrary points, the random variable is considered as the average value of those on the square vertices surrounding it.

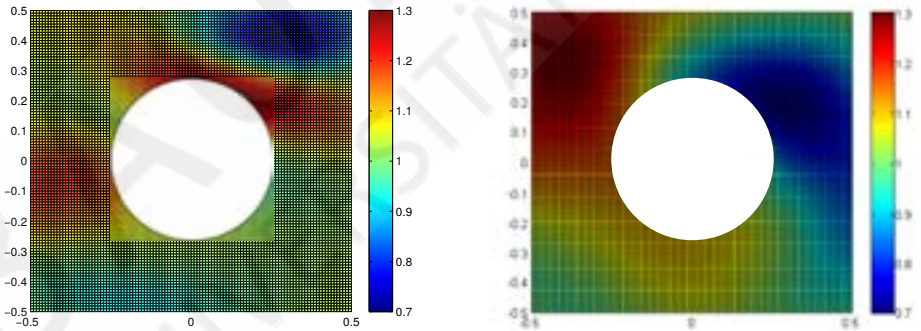

(a) (b)

FIGURE 6.23: Random field in the range [0.7,1.3] produced by the Gauss correlation variables: (a) [0.03, 0.01] and (b) [0.05, 0.04].

Like before, the reference solution is obtained by calculating the average of stress on the surface S at the finest mesh obtained by the goal-oriented adaptivity. The reference solutions for random fields 1 and 2 are $\sigma_{yy}^{av}|_S = -8,597,010$ and $\sigma_{yy}^{av}|_S = -9,137,850$, obtained by applying 236,466 and 236,200 degrees of freedom, respectively.

The relative errors of $\sigma_{yy}^{av}|_S$ for all the simulations are depicted in Figs. 6.24 and 6.25 for

random fields 1 and 2, respectively. The convergence rate of adaptivity based on GOEE tends is the highest among other conventional approaches.

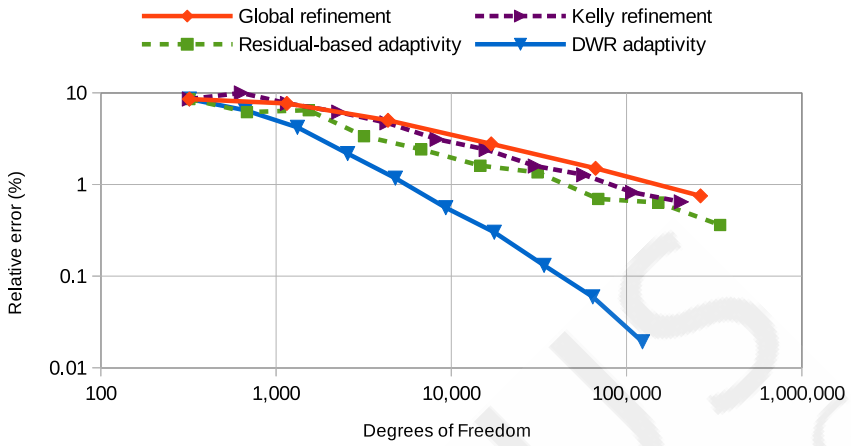

FIGURE 6.24: Relative errors (%) of $\sigma_{yy}^{av}|_S$ in heterogeneous concrete (produced by random field 1) under pressure.

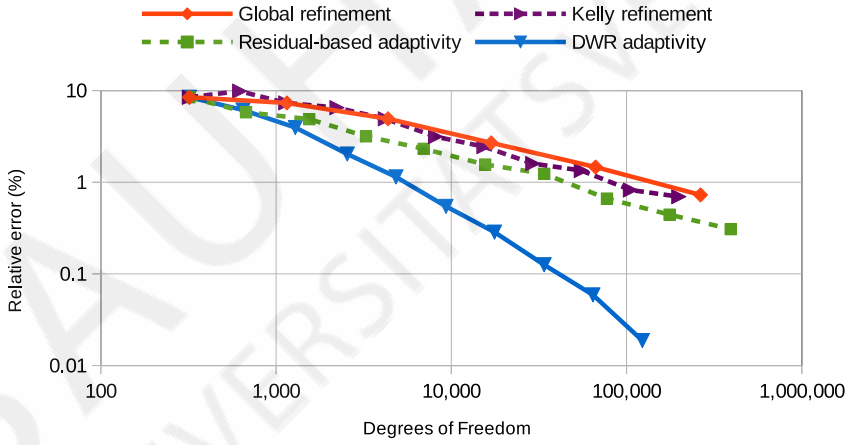

FIGURE 6.25: Relative errors (%) of $\sigma_{yy}^{av}|_S$ in heterogeneous concrete (produced by random field 2) under pressure.

In order to demonstrate the effect of different heterogeneities on the produced meshes applying different adaptivity approaches, mesh discretization of the fourth adaptivity step of all the simulations are presented in Fig. 6.26.

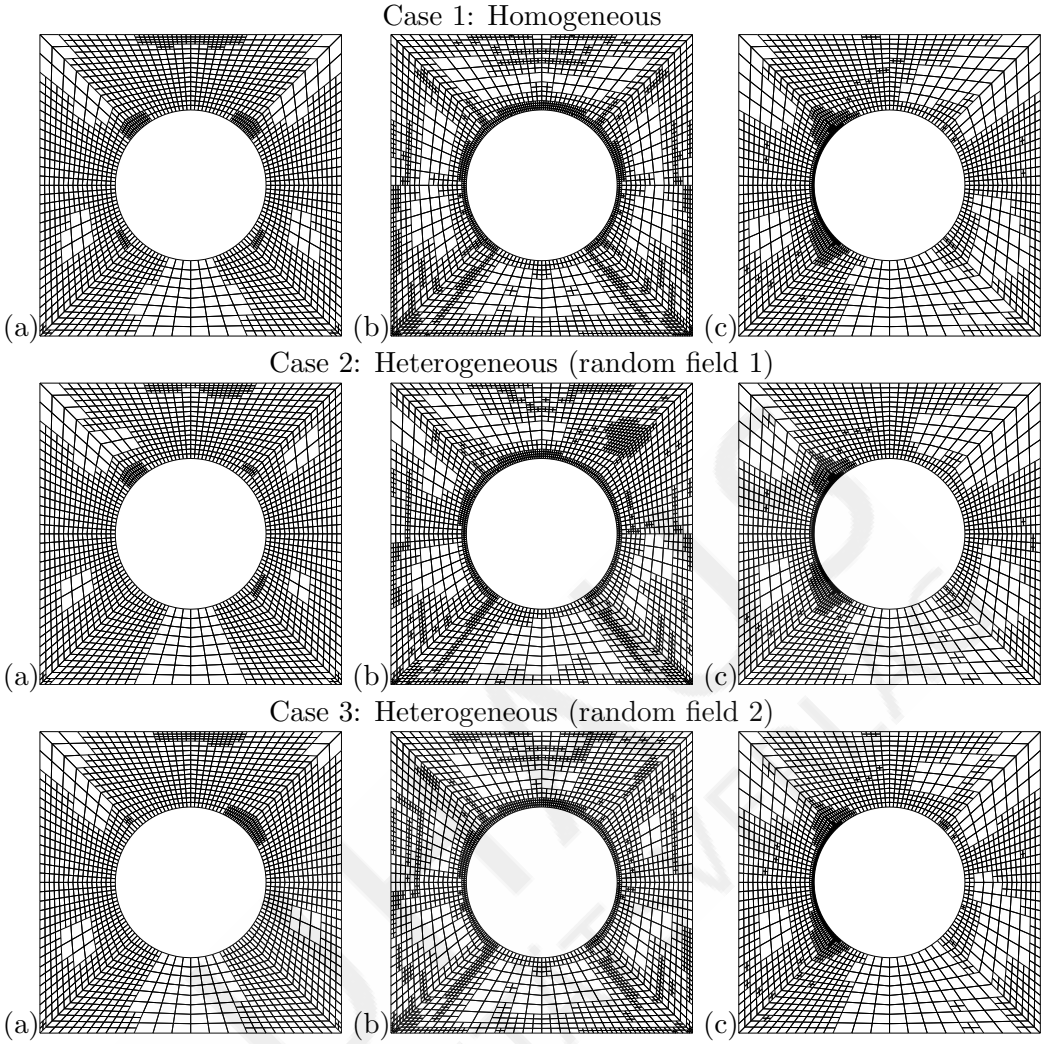

FIGURE 6.26: Meshes at the 4-th adaptivity step of the sample with a hole under pressure in homogeneous and heterogeneous cases by applying: (a) Kelly refinement, (b) residual-based adaptivity and (c) goal-oriented adaptivity.

6.1.4 3d elasticity problem [30]

In this section, a three-dimentional linear elasticity problem is considered. A solid with a cylindrical hole is subjected to a uniaxial traction P, as shown in Fig. 6.27(a). Due to symmetry, only a quarter of the solid is modeled (See Fig. 6.27(b)). The edge lengths of the solid are $2a$ and its thickness is a, where a is the radius of the cylindrical hole. The following constant values are considered: modulus of elasticity $E = 200$ GPa, Poissons ratio $\nu = 0.3$ and $P = 100$ MPa.

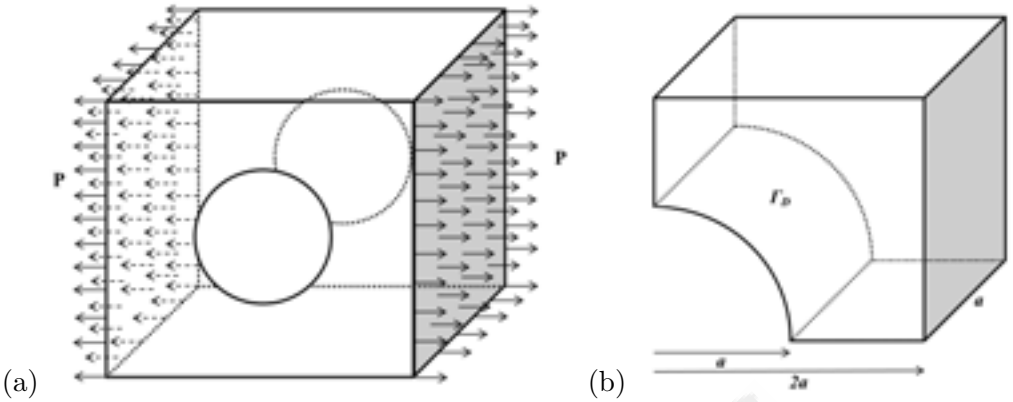

(a) (b)

FIGURE 6.27: (a) A three-dimentional infinite plate with a circular hole, (b) Quarter of 3D plate and surfaces for QoIs.

6.1.4.1 Global mesh adaptivity

Initial and refined mesh configurations with 675, 4131, 28611 and 212355 number of degrees of freedoms (DoFs) with 3 DoFs per node (u_x, u_y, u_z) are shown in Fig. 6.28. In this refinement procedure, in each step, an element is uniformly devided to 8 new elements.

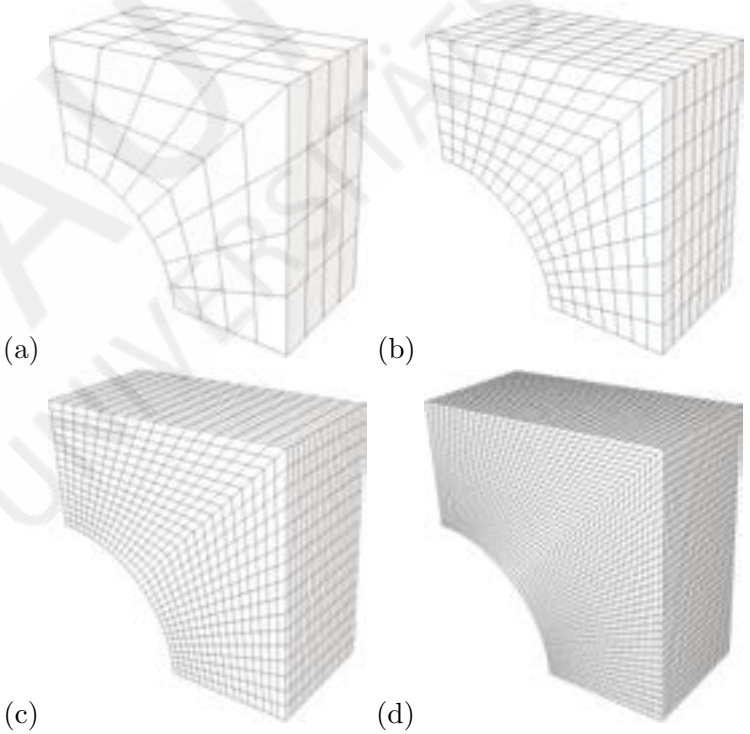

(a) (b)

(c) (d)

FIGURE 6.28: Global mesh adaptivity: (a) Initial mesh with 675 DoFs, (b) Refined mesh (1st step) with 4131 DoFs, c) Refined mesh (2nd step) with 28611 DoFs, d) Refined mesh (3rd step) with 212355 DoFs.

6.1.4.2 Mesh adaptivity based on Kelly error indicator

Initial and refined mesh configurations with 675, 2094, 5667, 16902, 51285 and 145527 Dofs are shown in Fig. 6.29. The meshes are refined based on the kelly error indicator [28].

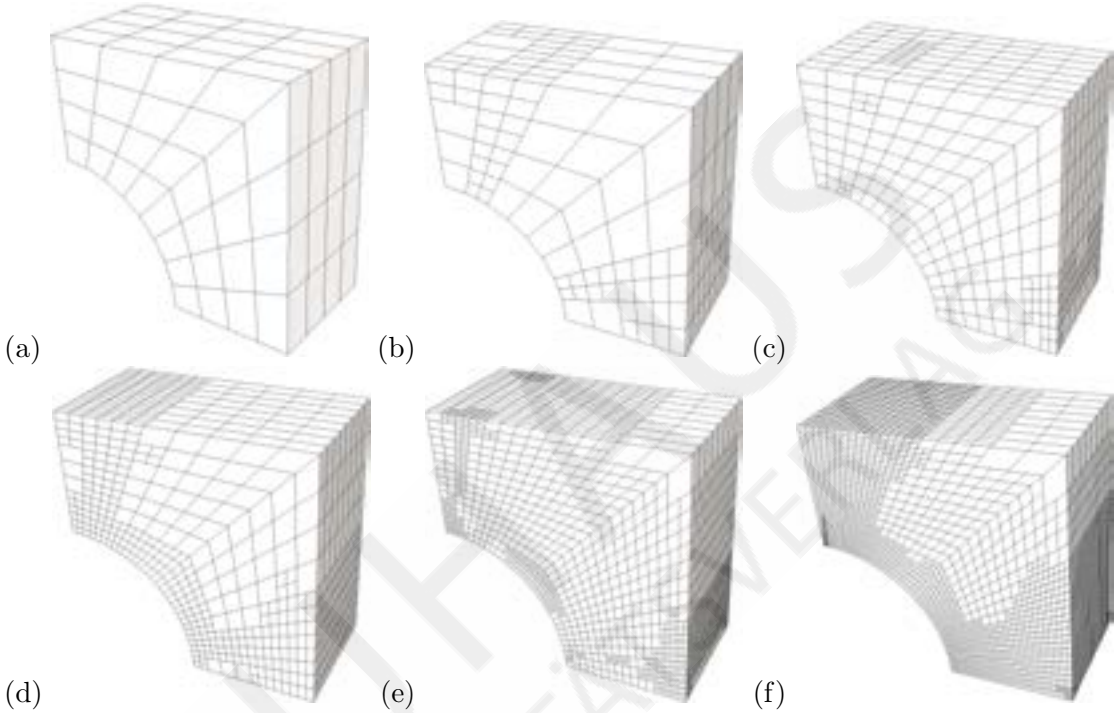

FIGURE 6.29: Mesh adaptivity based on Kelly error indicator, (a) Initial mesh with 675 DoFs, (b) Refined mesh (1st step) with 2094 DoFs, c) Refined mesh (2nd step) with 5667 DoFs, d) Refined mesh (3rd step) with 16902 DoFs, e) Refined mesh (4th step) with 51285 DoFs, f) Refined mesh (5th step) with 145527 DoFs.

6.1.4.3 Mesh adaptivity based on residual-based error estimation

Initial and refined nodal configurations with 675, 2178, 6786, 21567, 69081 and 229275 Dofs are shown in Fig. 6.30. The meshes are refined based on the residual-based error estimator described in Section 3.2.

6.1.4.4 Goal-oriented mesh adaptivity for mean σ_{xx} on Γ_D

The mean stress σ_{xx} on the curved surface Γ_D (see Fig. 6.27(b)) is considered as quantity of interest for the solution. The propsoed Goal-Oriented Error Estimation, GOEE, is

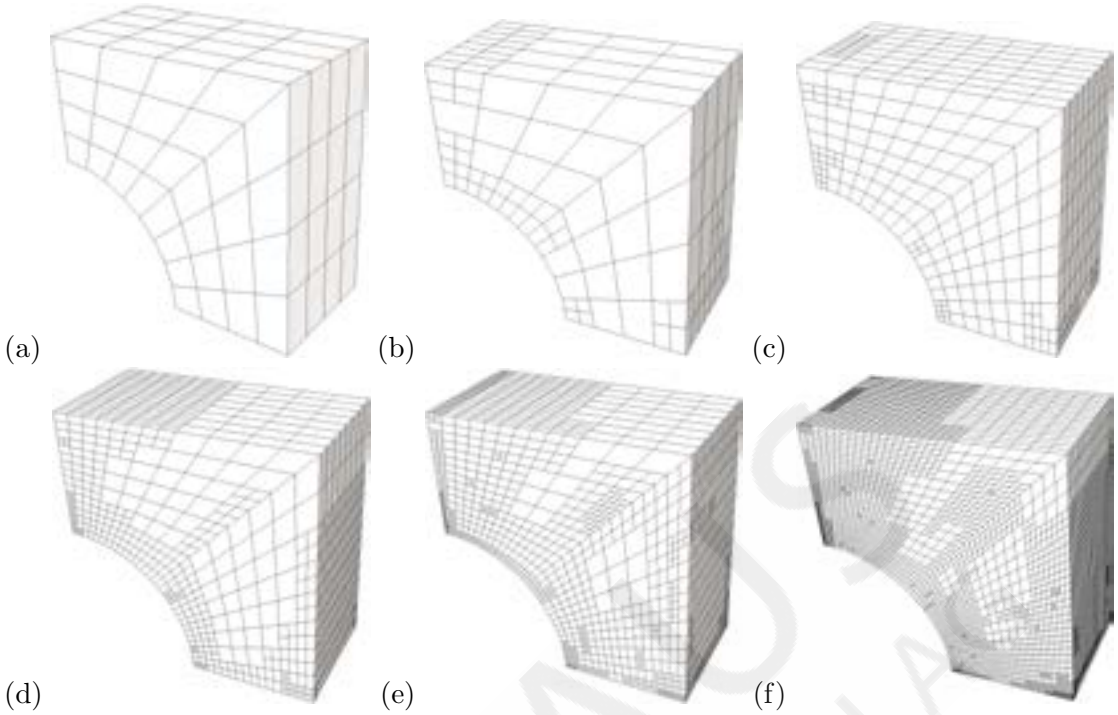

FIGURE 6.30: Mesh adaptivity based on residual-based error estimation, (a) Initial mesh with 675 DoFs, (b) Refined mesh (1st step) with 2178 DoFs, c) Refined mesh (2nd step) with 6786 DoFs, d) Refined mesh (3rd step) with 21567 DoFs, e) Refined mesh (4th step) with 69081 DoFs, f) Refined mesh (5th step) with 229275 DoFs.

applied for mesh adaptivity. Initial and refined mesh configurations with 675, 2292, 6771, 18282 and 58323 Dofs are shown in Fig. 6.31.

6.1.4.5 Comparison of convergence rates

The mean σ_{xx} on Γ_D in the finest solution of the Goal-Oriented Mesh Adaptivity (GOMA) procedure is considered as the approximation of the exact QoI. Considering that, the approximated errors of QoI for different mesh configurations obtained by appling different mesh adaptivity procedures are illustrated in Fig. 6.32(a). The corresponding convergence rates are also plotted in Fig. 6.32(b). While the obtained convegence rate of the GOMA procedure is 0.65, other refinement procedures based on residual error estimator, Kelly error indicator and global refinement results in the convergence rates 0.45, 0.37 and 0.33, respectively. The results clearly show the superiority of the GOEE in mesh adaptation over other conventional error estimation approaches where a specified quantity is of interest.

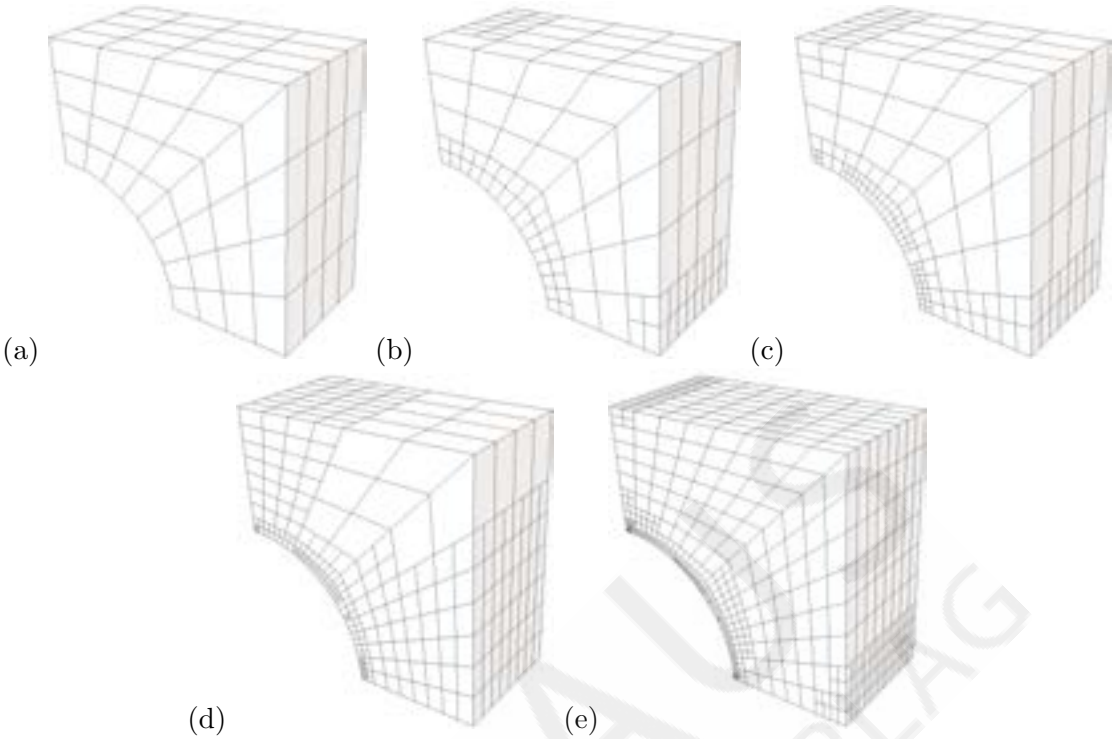

(a) (b) (c)

(d) (e)

FIGURE 6.31: Goal-oriented mesh adaptivity considering mean σ_{xx} on Γ_D as QoI: (a) Initial mesh with 675 DoFs, (b) Refined mesh (1st step) with 2292 DoFs, c) Refined mesh (2nd step) with 6771 DoFs, d) Refined mesh (3rd step) with 18282 DoFs, e) Refined mesh (4th step) with 58323 DoFs.

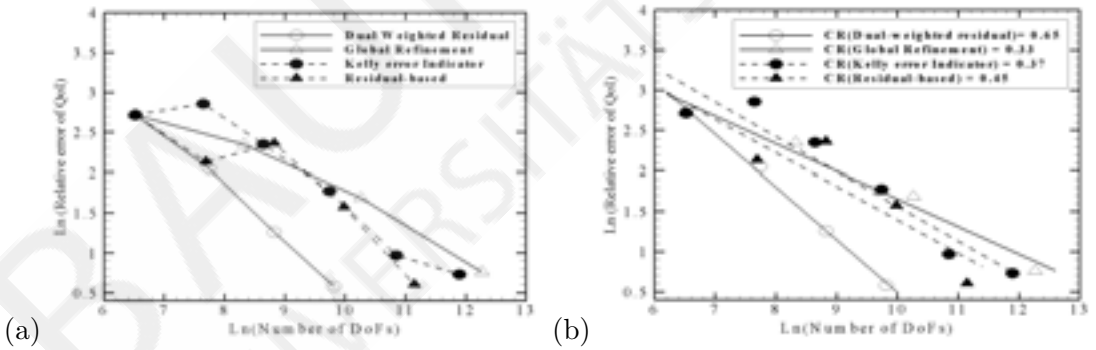

(a) (b)

FIGURE 6.32: Approximated errors of the QoI, mean σ_{xx} on Γ_D: (a) Convergence curve and (b) Convergence rate.

6.2 Elastoplasticity Problems

6.2.1 Thick tube subjected to internal pressure [31]

In order to verify the proposed approach in elastoplasticity, an example with available analytical solution is considered. Consider an elastic perfectly plastic thick tube in the

plane strain state subjected to uniform internal pressure. As a result of the geometry and loading symmetries, one quarter is only modeled (see Fig. 6.33).

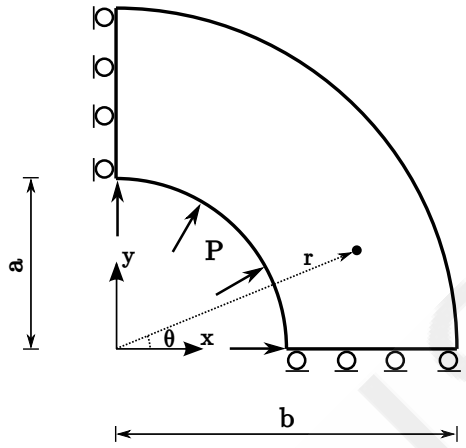

FIGURE 6.33: Geometry and boundary conditions of the thick tube subjected to uniform internal pressure.

The following geometry and material parameters are considered: Inner radius $a = 100$ mm, outer radius $b = 200$ mm, yield strength $\sigma_y = 240$ MPa, Young's modulus $E = 210$ GPa and Poisson's ratio $\nu = 0.3$.

If the imposed internal pressure, P, is sufficiently small, the entire tube remains elastic. However, when P becomes large enough, the tube begins to yield from the inner surface $r = a$. With the continuous increase of P the yielded region will expand outwards. From symmetry it follows that the elasto-plastic interface is also a cylindrical surface for any value of P that produces a plastic region. Let r_c be the radius of this elasto-plastic interface, and P_c be the associated pressure acting on the interface under P (a generic value). Then, the material in the region $a \leq r \leq r_c$ is in the plastic state, whereas the material in the region $r_c \leq r \leq b$ remains elastic under P.

The radius of elasto-plastic interface, r_c, can be calculated by solving the following equation [45],

$$P = \frac{\sigma_y}{\sqrt{3}} \left[1 - \frac{r_c^2}{b^2} + 2 \ln \frac{r_c}{a} \right], \tag{6.3}$$

where σ_y is the yield strength of the material; a and b are the inner and outer radii of the model, respectively.

The analytical stress and displacement solutions in the polar coordinates for the plastic and elastic regions, are as follows:

- Plastic region ($a \leq r \leq r_c$):

$$\sigma_{rr} = \frac{\sigma_y}{\sqrt{3}}\left[-1 + \frac{r_c^2}{b^2} - 2\ln\frac{r_c}{r}\right], \qquad \sigma_{\theta\theta} = \frac{\sigma_y}{\sqrt{3}}\left[1 + \frac{r_c^2}{b^2} - 2\ln\frac{r_c}{r}\right] \tag{6.4}$$

$$u_r = \frac{\sqrt{3}}{2}\frac{\sigma_y}{E}\frac{r_c^2}{r}. \tag{6.5}$$

- Elastic region ($r_c \leq r \leq b$):

$$\sigma_{rr} = \frac{P_c r_c^2}{b^2 - r_c^2}\left(1 - \frac{b^2}{r^2}\right), \qquad \sigma_{\theta\theta} = \frac{P_c r_c^2}{b^2 - r_c^2}\left(1 + \frac{b^2}{r^2}\right), \tag{6.6}$$

$$u_r = \frac{1+\nu}{E}\frac{P_c r_c^2}{b^2 - r_c^2}\left(1 - 2\nu + \frac{b^2}{r^2}\right) r \tag{6.7}$$

where P_c is the pressure on the elasto-plastic interface, $r = r_c$, which can be calculated from Eq. (6.4),

$$P_c = -\sigma_{rr}|_{r=r_c} = -\frac{\sigma_y}{\sqrt{3}}\left[-1 + \frac{r_c^2}{b^2}\right]. \tag{6.8}$$

The initial discretization (192 elements) is shown in Fig. 6.34. Several simulations with constant load increments, $\Delta P = 1, 6, 24, 192$ MPa, are performed.

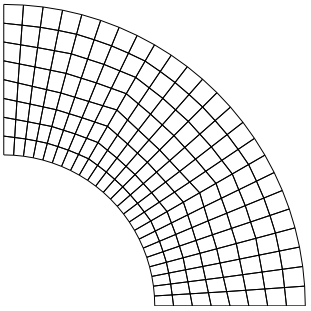

FIGURE 6.34: Initial discretization for modeling the thick tube.

Fig. 6.35 demonstrates the variation of load factor P/σ_y with the non-dimensionalized displacement $4\mu u_a/(\sigma_y a)$ at the inner radius for different load increment steps besides the theoretical solution [45], obtained by using Eqs. (6.3), (6.7) and (6.5). μ is shear modulus and u_a is the radial displacement at the inner radius $r = a$. A slight discontiuity is observed in the analytical solution when the inner radius enters the plasticity, $r_c = 0.1$ and $P/\sigma_y = 0.433013$, since the plastic deformation formulations were derived with the assumption of incompressibility. It is seen that the numerical results are in good agreement with analytical solutions. Elements of the first layer of the model, with incremental load $\Delta P = 1$ MPa, enters into plasticity when $P = 113$ MPa. Then, as the load increases, the elastic elements enters into plastic zone gradually and the whole model becomes plastic when $P = 194$ MPa.

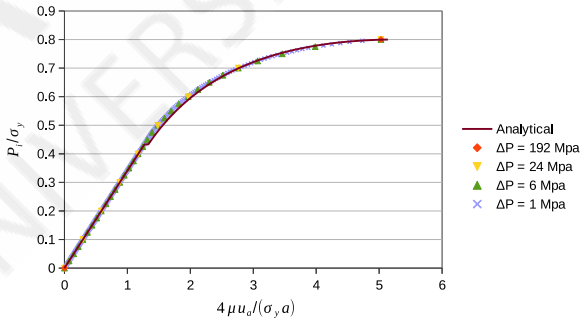

FIGURE 6.35: Non-dimensional load-displacement curve in the thick tube model.

Table 6.1 presents the non-dimensionalized load and displacement values as well as their corresponding exact error (%) for the case $\Delta P = 6$ MPa.

Fig. 6.36 illustrates the distribution of radial and hoop stresses along the radius for

TABLE 6.1: Non-dimensionalized load and displacement values and their errors (%) for the case $\Delta P = 6$ MPa

Load step	$\frac{P}{\sigma_y}$	$\frac{4\mu u_a}{\sigma_y a}\|_{\text{simulation}}$	$\frac{4\mu u_a}{\sigma_y a}\|_{\text{analytical}}$	Exact error (%)
1	0.1	0.2926	0.293333	0.25
2	0.2	0.5852	0.586667	0.25
3	0.3	0.8778	0.88	0.25
4	0.4	1.1703	1.173333	0.26
5	0.5	1.4822	1.562204	5.12
6	0.6	1.9657	2.026866	3.02
7	0.7	2.7618	2.771664	0.36
8	0.8	5.0289	5.138994	2.14

$P/\sigma_y = 0.6$. The presented stresses are the nodal stresses computed from nodal avarag-ing technique. For their computation, firstly the stresses on the Gauss points are trans-formed to the polar coordinates, then they are extrapolated to the nodes. Since at each node different values may be obtained from the adjacent elements, the average value is computed. The results agree well with the analytical solutions. The errors at the inner radius, $r = a$, are maximum and it is expected that more refinement near the inner radius, leads to higher accuracy.

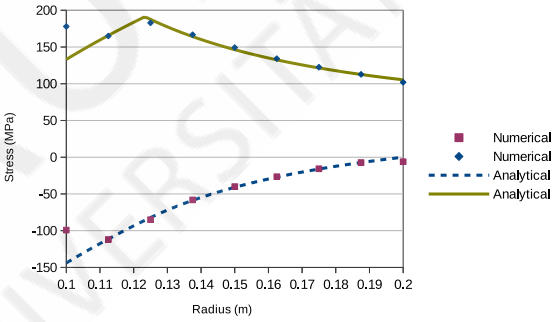

FIGURE 6.36: Distribution of σ_{rr} and $\sigma_{\theta\theta}$ (MPa) along radial direction for $P/\sigma_y = 0.6$.

Now, suppose that we intend to increase the accuracy in the numerically calculated stresses on the inner curve S when $P/\sigma_y = 0.6$. The corresponding functional, which is substituted in the right-hand side of Eq. (4.8), can be defined as

$$J(\mathbf{v}) = \frac{1}{|\Gamma_S|}\int_{\Gamma_S}\sum_{i,j}\sigma_{ij}(\mathbf{v})d\Gamma, \qquad i,j = x,y\,, \tag{6.9}$$

where $|\Gamma_S|$ is the arc length S with radius, $r = 0.1$.

Incremental load $\Delta P = 24$ MPs is imposed. As a starting point of the adaptivity process, 48 elements (130 DoFs) are applied for the discretization (see Fig. 6.37 (a)). Different strategies including global refinement and adaptivity based on estimated errors by using Kelly, residual and goal-oriented error estimation, GOEE, have been tested. Each methodology leads to different element errors and therefore, the resulting meshes are different. Figs. 6.37 (b-d) illustrate the sample resulting meshes of different schemes. Fig. 6.37 (c) shows a non-uniform distribution of elements, probably due to the kinks along the element boundaries at the angles $\theta = 30\,^\circ$ and $\theta = 60\,^\circ$. The GOEE-based adaptivity leads to mesh concentration around the surface S where the quantity of interest has been defined.

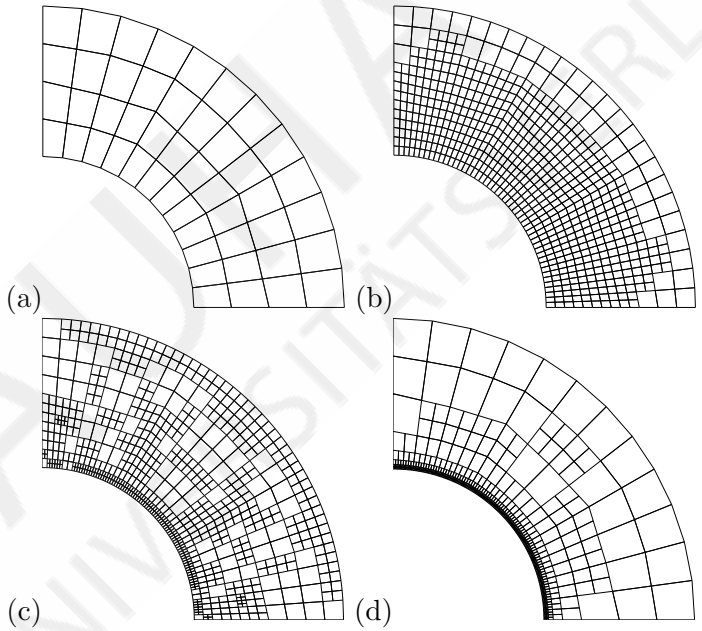

FIGURE 6.37: Discretizations of the thick tube model: (a) Initial mesh; meshes resulted in adaptivity process applying (b) Kelly error estimation with 630 elements, (c) Residual error estimation with 684 elements and (c) GOEE with 618 elements.

The relative errors in the $\sigma^{av}_{rr}|_S$ are depicted in Fig. 6.38. The goal-oriented error estimation results in an adaptivity process with better convergence rate. Very similar results are obtained for the $\sigma^{av}_{\theta\theta}|_S$.

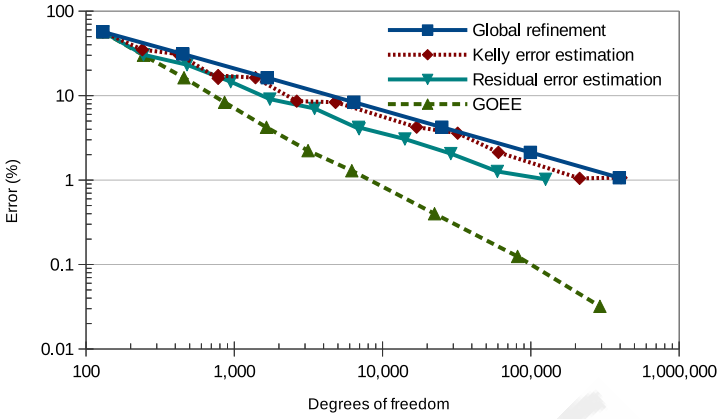

FIGURE 6.38: Exact relative errors (%) of $\sigma_{rr}^{av}|_S$ versus degrees of freedom for the thick wall subjected to internal pressure.

Fig. 6.39 illustrates the exact relative error (%) of $\sigma_{rr}^{av}|_S$ versus the consumed computational time (sec). It is shown that for achieving a precise solution of the quantity of interest, the proposed goal-oriented adaptivity is the most efficient method.

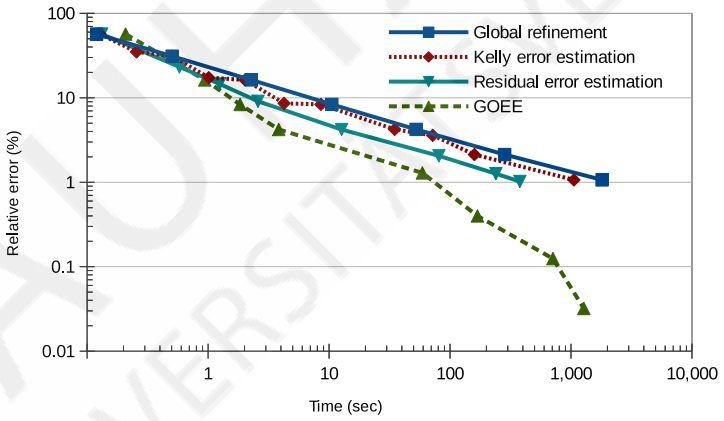

FIGURE 6.39: Exact relative errors (%) of $\sigma_{rr}^{av}|_S$ versus computational times (sec) for the thick wall subjected to internal pressure.

6.2.2 Round perforated strip under enforced displacement [31]

Consider the perforated strip of strain-hardening material, which was studied experimentally by Theocaris and Marketos [46]. Due to the symmetry only a quarter of the strip is modeled (see Fig. 6.40), with length $L = 180$ mm, width $W = 100$ mm, perforation radius $R = 50$ mm and thickness $T = 4$ mm. The material used was an aluminium

alloy 57S with a yield stress in pure tension $\sigma_y = 243$ MPa. Other material parameters are: Elastic modulus $E = 70$ GPa, Poisson's ratio $\nu = 0.3$ and plastic modulus $\gamma^{iso} = 2\mu\frac{\gamma}{1-\gamma} = 2.25$ GPa which leads to $\gamma = 0.0401097$.

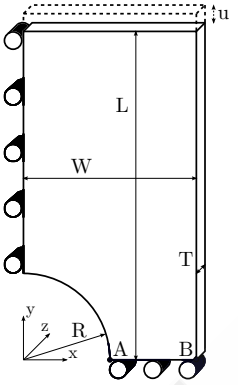

FIGURE 6.40: Geometry and loading of a perforated strip subjected to imposed displacement.

The mean stress component σ_{yy} on the bottom surface S, where $y = 0$, is considered as the quantity of interest:

$$J(\mathbf{v}) = \frac{1}{|\Gamma_S|}\int_{\Gamma_S} \sigma_{yy}(\mathbf{v})d\Gamma\,, \tag{6.10}$$

where $|\Gamma_S|$ is the area of the surface S.

A displacement $u_y = 0.55$ mm as shown in Fig. 6.40 is imposed at the top surface incrementally in 22 steps. The initial mesh consisting of 192 elements and the goal-oriented refined mesh composed of 1830 elements are shown in Fig. 6.41.

Fig. 6.42 illustrates the relation between the non-dimensional average stress on the bottom surface, $\sigma^{av}_{yy}/\sigma_y$, and the non-dimensional strain at the point A, $E\varepsilon^A_{yy}/\sigma_y$. Fig. 6.42 also includes the experimental results which were extracted by reading the values from the plots provided in [46].

The computed strain is larger than the experimentally observed strain. Other invistigators reported similar discrepancies. A possible explanation is that in the case of the

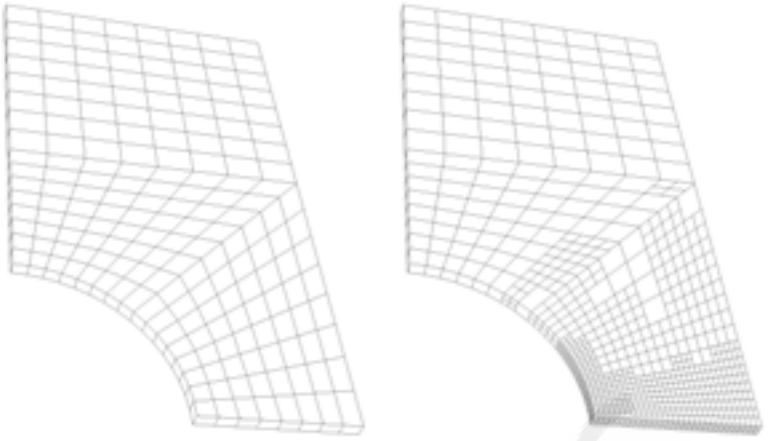

(a) (b)

FIGURE 6.41: Discretization of the perforated strip subjected to imposed displacement: (a) Initial mesh (192 elements); (b) Refined mesh applying Goal-oriented adaptivity (1830 elements).

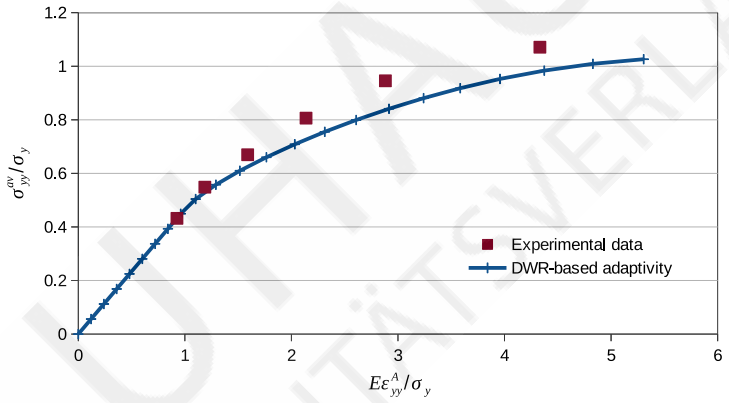

FIGURE 6.42: Non-dimensional relation between σ^{av}_{yy} and ε_{yy} at Point A.

numerical simulation the strain is reported with an infinitesimal gauge length whereas experimentally determined strains invariably involve some gauge length of finite size.

Fig. 6.43 depicts the distribution of normalized stress σ_{yy}/σ_y along AB ($y = z = 0$) at step 19 where the imposed displacement is $u_y = 0.475$ mm. The results are in good agreement with experimental data [46]. The σ_{yy} stress distribution at the same step is also illustrated in Fig. 6.44 for the whole domain.

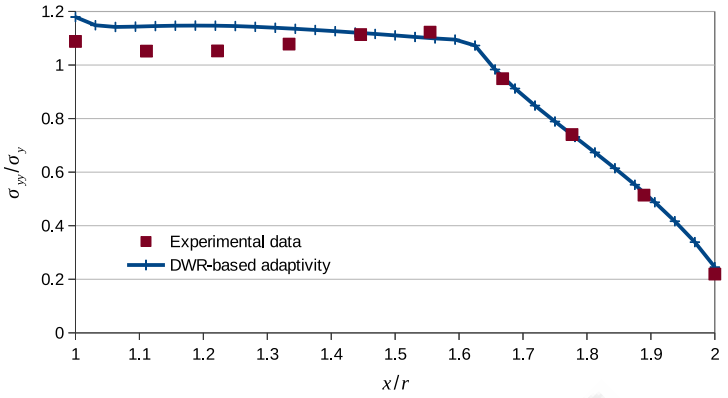

FIGURE 6.43: Distribution of non-dimensional tensile stress σ_{yy} along AB at step 19 where the imposed displacement is $u_y = 0.475$ mm.

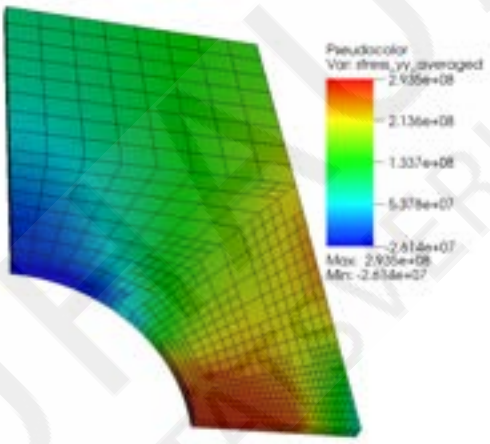

FIGURE 6.44: Distribution of stress component σ_{yy} at step 19 where the imposed displacement is $u_y = 0.475$ mm.

6.2.3 Cantiliver beam under surface pressure [31]

Consider a rectangular tube made of aluminium alloy 57S, which is clamped at one end and subjected to surface pressure. The material is the same as in the previous example. The geometry and loading is shown in Fig. 6.45 with Length, $L = 70$ cm, width, $W = 8$ cm, height, $H = 20$ cm, web and flange thicknesses, $t_w = t_f = 1$ cm and surface pressure, $P = 6$ MPa.

In this example two different quantities of interest, QoI, are considered separately for the goal-oriented mesh adaptivity.

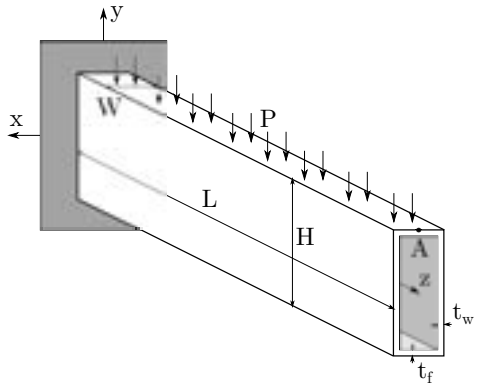

FIGURE 6.45: Geometry and loading of a cantiliver beam subjected to pressure on the top surface.

The first QoI is the displacement at Point A, $\mathbf{u}_A$, located in $x = 0, y = H/2, z = L$ (see Fig. 6.45). Accurate prediction of this QoI leads to a more precise load deflection curve which is important in materials design. By using the definition of the Dirac delta function, δ, the corresponding functional is defined as

$$J(\mathbf{v}) = \mathbf{v}(\mathbf{x}_A) = \int_\Omega \mathbf{v}\delta(\mathbf{x} - \mathbf{x}_A)d\Omega\,. \tag{6.11}$$

Now, consider that we want to calculate the maximum von-Mises stress in the beam which is important to predict the failure load accurately. Knowing that the maximum von Mises stress occurs at the flanges close to the clamped area, we define the QoI functional as the average value of all stress components in the domain, Ω_V, which consists of the first row of elements (in initial mesh) in top and bottom flanges closed to the fixed area, $-W/2 \leq x \leq W/2$, $H/2 - t_f \leq y \leq H/2$, $-H/2 \leq y \leq -H/2 + t_f$, $0 \leq z \leq 2t_f$,

$$J(\mathbf{v}) = \frac{1}{|\Omega_0|}\int_{\Omega_0}\sum_{i,j}\sigma_{ij}(\mathbf{v})d\Omega, \qquad i,j = x,y,z\,, \tag{6.12}$$

and its corresponding linearized form is defined as

$$J^{lin}(\mathbf{v}) \;=\; \frac{1}{|\Omega_0|}\int_{\Omega_0}\sum_{i,j}\nabla\sigma_{ij}(\mathbf{u}^h)\cdot\mathbf{v}d\Omega, \qquad i,j = x,y,z\,. \tag{6.13}$$

The surface pressure P is applied in 10 loading steps. The mesh discretization consisting of 1820 elements shown in Fig. 6.46(a) is considered as the initial mesh. Global refinement and local refinement based on elementwise errors computed by applying Kelly, residual-based and goal-oriented error estimations are performed in 1-2 levels.

Fig. 6.46 shows the initial mesh and two-level adapted meshes resulted of applying different error estimations. In all cases except for the GOEE-based refinement, the refinement is performed in the first step and the computed errors in the rest steps remained below the specified value. In the GOEE-based refinement case based on the first QoI, $|u_y^A|$, the specified maximum relative error, 4.4e-5, leads to a refinemnt level in the first step and the second refinment level in the seventh step (see Fig. 6.46(d)). It is noted that the unsymmetrical meshes in Fig. 6.46(d) with respect to y-axis is the result of the unsymmetric dual problem, which determines the elementwise weights which affect the quality assessment of the $|u_y^A|$.

Fig. 6.47 illustrates the load-deflection curve for initial mesh and global refinement cases. The number of degrees of freedom are 11 232, 66 456 and 439 920, respectively, for uniform refinements. It is observed that the results converges with increasing refinement.

The results of $|u_y^A|$ for all load steps and refinement strategies are given in Table 6.2. If we consider the computed $|u_y^A|$ in the global refinement 2, as the most accurate result which can be achieved in two refinement levels, it is observed that the Goal-oriented mesh adaptivity procedure results in more accurate result in comparison with other applied refinement methodologies.

The GOEE-based mesh adaptivity is also performed considering the second QoI and a prescribed maximum permissible error. Accordingly, refinement has been performed in the 6^{th} and 8^{th} steps. The mesh discretization in the 8^{th} is depicted in Fig. 6.46(e). Fig. 6.48 demonstrates the von-Mises stress distribution and the plastic zones at the 8^{th} loading step where the imposed pressure is $P = 4.8$ MPa.

If we consider the maximum von-Mises stress computed in the two-level global refinement as the reference solution, we can compare the accuracy of GOEE results with those

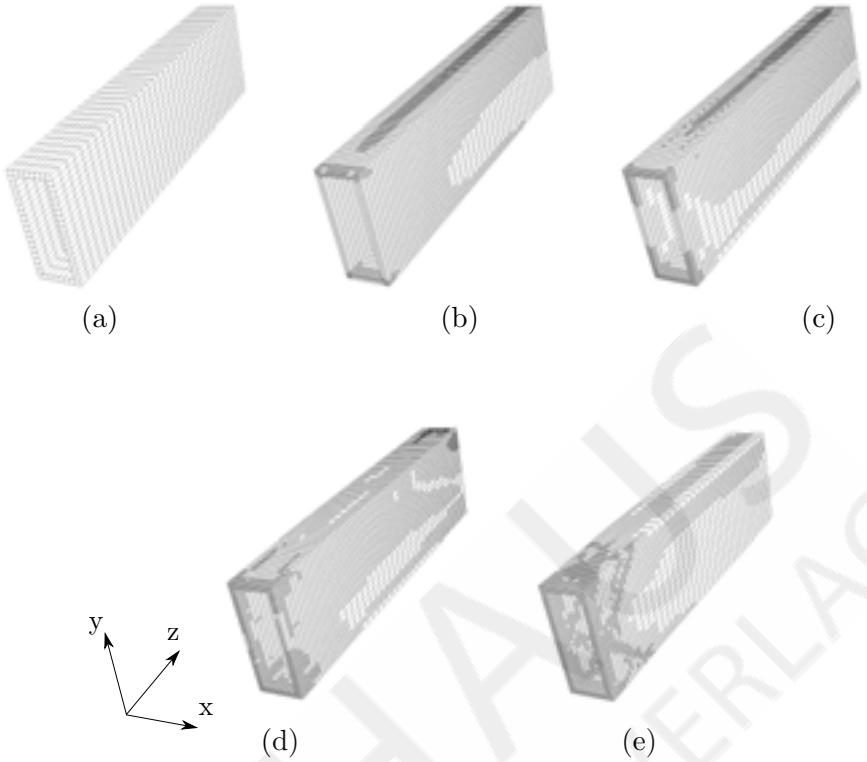

FIGURE 6.46: Discretization of the cantiliver beam of rectangular tube: (a) Initial mesh (1 820 elements); Two-level refined meshes applying (b) Kelly error estimation(17 486 elements), (c) residual-based error estimation (17 500 elements), (d) GOEE (17 472 elements in step 8) considering the first QoI and (e) GOEE (17 486 elements in step 8) considering the second QoI.

obtained by applying Kelly and residual-based error estimations. The corresponding relative errors of each model at loading steps 8-10 are given in Table 6.3. Comparison of results highlights the superiority of the proposed approach compared to the other conventional mesh refinement procedures.

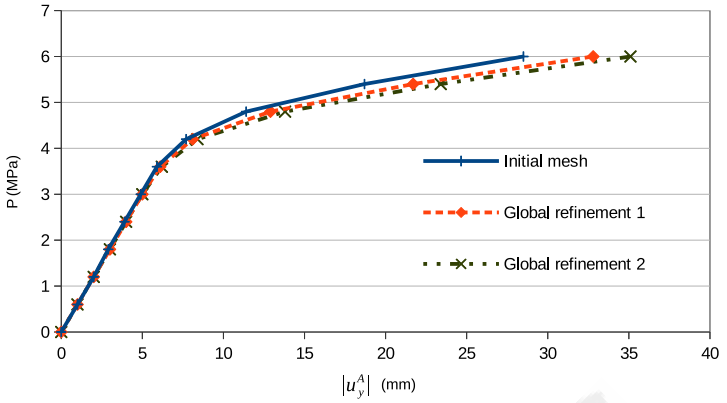

FIGURE 6.47: Relation between pressure, P, and absolute value of displacement at point A in y direction, $|u_y^A|$ for different global refinement.

TABLE 6.2: Resulted $|u_y^A|$ (mm) for different loading steps by applying several refinement strategies

Elements / LS	IM 1820	GR 1 14560	GR 2 116480	KR 1 5642	KR 2 17486	RR 1 5642	RR 2 17500	GOEE 5642, 17472
1	1	*1	**1	*1	**1	*1	**1	*1
2	2	2	2	2	2	2	2	2
3	2.9	3	3	3	3	3	3	3
4	3.9	4	4	4	4	4	4	4
5	4.9	5	5	4.9	5	4.9	5	4.9
6	5.9	6.1	6.2	6.1	6.1	6.1	6.1	6.1
7	7.7	8.1	8.4	8.1	8.2	8	8.3	**8.3
8	11.4	12.9	13.8	12.7	13.2	12.5	13.4	13.6
9	18.7	21.7	23.4	21.4	22.4	21.1	22.8	23
10	28.5	32.8	35.1	32.4	33.7	32.1	34.3	34.6

LS: Load step, IM: Initial mesh, GR: Global refinement,
KR: Kelly-based refinement, RR: Residual-based refinement,
*: First refinement step, **: Second refinement step

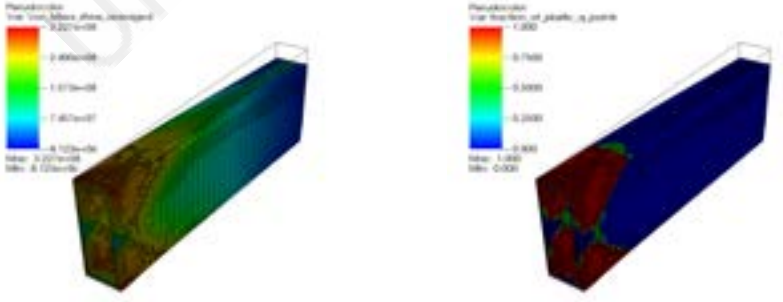

(a) (b)

FIGURE 6.48: (a) Von-Mises stress distribution and (b) Plastic zones: at 8th step computed by applying the goal-oriented mesh adaptivity. Displacements have been magnified by 3.

TABLE 6.3: Relative error of maximum von-Mises stress (%) at loading steps 8-10 considering the solution in two-level global refined case as the reference solution.

	KR 2	RR 2	GOEE
Elements	17 486	17 500	17 486
Load step			
8	3.42	1.36	0.19
9	4.82	1.66	0.20
10	5.61	1.61	0.14

KR: Kelly-based refinement, RR: Residual-based refinement

Chapter 7

Conclusion

In the finite element method, mesh discretization highly affects the solution accuracy and obviously the computational effort. An error estimation method should be performed to locate the error distribution in the problem domain. A mesh adaptivity procedure is a key to achieve high accuracy result with minimum computational cost. It applies the local estimated errors to achieve an optimal mesh configuration.

In this thesis, a goal-oriented error estimation approach has been applied to 2d elasticity problems with heterogeneous material and further extended to 3d elasticity and elastoplasticity problems for estimating element-wise errors in a quantity of interest. Consequently, an automatic mesh adaptivity procedure, including hierarchical refinement and coarsening has been utilized to control the local errors in the quantity of interest. In order to show the advantages of goal-oriented error estimation, two conventional recovery-based and residual-based error estimations, which estimates the errors in energy norms, have also been performed.

The applied goal-oriented error estimation approach is called dual-weighted residual, which is the weighted form of the residual-based error estimation. The weighted factors are computed according to the solution of a dual problem which is defined based on the quantity of interest.

Definition of the dual problem is different in elasticity and elastoplasticity problems. In the elasticity problem, the dual problem is defined independent of the primal problem, therefore they can be solved in parallel. In the elastoplasticity problem, the dual problem is constructed according to the primal solution, but is defined as a linear problem. So, it amounts only to a small fraction of the total cost within the Newton iteration for the nonlinear primal problem. In order to do the goal-oriented mesh adaptivity in elastoplasticity problem, the error is computed at each load/displacement increment and when it is greater than the prescribed maximum error, mesh adaptivity is performed and the solution is projected from the old mesh to the new mesh.

In order to do the mesh adaptivity, local refinement and coarsening utilizing tetrahedral and hexahedral elements in 2d and 3d problems, respectively, have been applied. Correspondingly, hanging nodes are introduced which are constrained to be compatible with the adjacent nodes.

The proposed automatic continuous goal-oriented mesh adaptivity has been applied in several 2d and 3d numerical examples with elastic and elastoplastic material considering different quantities of interest. Its accuracy, efficiency and performance have been investigated by comparing the results with available analytical solutions, existing experimental data and the results of mesh adaptivity based on other typical error estimation methods.

It is seen that different error estimations present dissimilar local error distributions and therefore, application of mesh adaptivity results in different mesh configurations.

It is observed that when a specific quantity is of interest rather than the solution in the whole domain, application of the proposed goal-oriented mesh adaptivtiy leads to high accuracy with less elements/degrees of freedom (higher convergence rate).

The corresponding code has been written in C++ programming language within the framework of the deal.II library [32, 33] and is available online as an open source code. Therefore, the readers will be able to apply the proposed approach and it's further application and developments will be more convenient. One important application would

be analysis and design of composite materials consisting of elastoplastic components. Further development of the approach for model error estimation and model adaptation is worthwhile for verification and validation purposes.

Appendix A

Random Fields

It has become state of the art to model the spatial variability of a material by random fields. The generated fields have in common that indeed the material properties at any point are random, however a certain correlation between neighboring points is accounted for to avoid naturally non realistic rapid changes. There are different strategies to generate random fields, e.g. for their use in Finite Element Modeling, see [47]. The technique applied in this work bases on realizations of Gaussian random fields depending on a prescribed correlation structure. We are assuming stationary Gaussian fields with given mean μ and standard deviation σ. For modeling the variability of the field, we are using a covariance matrix approach including a Gaussian model. For a two dimensional situation the correlation function is linked to the covariance matrix $\mathrm{Cov}(\mathrm{X}, \mathrm{X}')$ by

$$\rho(\tau_1, \tau_2) = \frac{\mathrm{Cov}(\mathrm{X}, \mathrm{X}')}{\sigma_X \sigma_{X'}}$$

where σ_X and $\sigma_{X'}$ are the standard deviations of at the points X and X', which obtain, however, the same value due to the assumption of stationarity. According to a Gaussian model, the correlation function is given by

$$\rho(\tau_1, \tau_2) = \exp\left(-\frac{2|\tau_1|}{\theta_1}\right)\left(-\frac{2|\tau_2|}{\theta_2}\right)$$

which shares the Markovian assumption in each spatial direction. The parameters θ_1 and θ_2 are the correlation lengths and decide about the variability of the field. The computation of the field is achieved by a Choleski Decomposition of the covariance matrix. If Cov is a positive definite covariance matrix generated from a correlation function for any discretized field, then a zero mean field F can be computed by

$$F = LU$$

where L stems from an Choleski decomposition of Cov, i.e.

$$\mathrm{Cov} = \mathrm{LL}^{\mathrm{T}}$$

and U is a vector of independent zero mean normally distributed random variables with standard deviation of one. F is then an autocorrelated realization of the random field at a discrete set of points with covariance matrix Cov. An appropriate Matlab Package is written by [48] extending the work of [49] which was used to generate the fields as sketched in Figures 6.15 and 6.23.

Bibliography

[1] O.C. Zienkiewicz and R.L. Taylor. *The finite element method*, volume I. McGraw Hill, 1989.

[2] O.C. Zienkiewicz and R.L. Taylor. *The finite element method*, volume II. McGraw Hill, 1991.

[3] Vinh Phu Nguyen, Timon Rabczuk, Stéphane Bordas, and Marc Duflot. Meshless methods: A review and computer implementation aspects. *Mathematics and Computers in Simulation*, 79(3):763 – 813, 2008.

[4] T. Rabczuk and T. Belytschko. Cracking particles: a simplified meshfree method for arbitrary evolving cracks. *International Journal for Numerical Methods in Engineering*, 61(13):2316–2343, 2004.

[5] S.Sh. Ghorashi, S. Mohammadi, and S.-R. Sabbagh-Yazdi. Orthotropic enriched element free galerkin method for fracture analysis of composites. *Engineering Fracture Mechanics*, 78(9):1906 – 1927, 2011.

[6] H. Khazal, H. Bayesteh, S. Mohammadi, S.Sh. Ghorashi, and A. Ahmed. An extended element free galerkin method for fracture analysis of anisotropic functionally graded materials. *Mechanics of Advanced Materials and Structures*, 23(5):513–528, 2015.

[7] T.J.R. Hughes, J.A. Cottrell, and Y. Bazilevs. Isogeometric analysis: Cad, finite elements, nurbs, exact geometry and mesh refinement. *Computer Methods in Applied Mechanics and Engineering*, 194(39–41):4135 – 4195, 2005.

[8] S.Sh. Ghorashi, N. Valizadeh, and S. Mohammadi. Extended isogeometric analysis for simulation of stationary and propagating cracks. *International Journal for Numerical Methods in Engineering*, 89(9):1069–1101, 2012.

[9] Yue Jia, Cosmin Anitescu, Seyed Shahram Ghorashi, and Timon Rabczuk. Extended isogeometric analysis for material interface problems. *IMA Journal of Applied Mathematics*, 2014.

[10] S.Sh. Ghorashi, N. Valizadeh, S. Mohammadi, and T. Rabczuk. T-spline based {XIGA} for fracture analysis of orthotropic media. *Computers & Structures*, 147 (0):138 – 146, 2015. CIVIL-COMP.

[11] I. Babuška and W. C. Rheinboldt. A-posteriori error estimates for the finite element method. *International Journal for Numerical Methods in Engineering*, 12(10):1597–1615, 1978.

[12] O. C. Zienkiewicz and J. Z. Zhu. A simple error estimator and adaptive procedure for practical engineering analysis. *International Journal for Numerical Methods in Engineering*, 24(2):337–357, 1987.

[13] O. C. Zienkiewicz and J. Z. Zhu. The superconvergent patch recovery and a posteriori error estimates. part 1: The recovery technique. *International Journal for Numerical Methods in Engineering*, 33(7):1331–1364, 1992.

[14] O. C. Zienkiewicz and J. Z. Zhu. The superconvergent patch recovery and a posteriori error estimates. part 2: Error estimates and adaptivity. *International Journal for Numerical Methods in Engineering*, 33(7):1365–1382, 1992.

[15] R. Becker and R. Rannacher. A feed-back approach to error control in finite element methods: Basic analysis and examples. *East-West Journal of Numerical Mathematics*, 4:237–264, 1996.

[16] R. Becker and R. Rannacher. Weighted a posteriori error control in fe methods. In Bock, H. G. et al., ed.s, ENUMATH 95, pages 621–637, Paris, September 1998. World Scientific Publ., Singapore., 1998.

[17] W. Bangerth and R. Rannacher. *Adaptive finite element methods for differential equations*. Birkhäuser Verlag, Basel, 2003.

[18] S. Prudhomme and J.T. Oden. On goal-oriented error estimation for elliptic problems: application to the control of pointwise errors. *Computer Methods in Applied Mechanics and Engineering*, 176(1–4):313 – 331, 1999.

[19] E. Stein, M. Rüter, and S. Ohnimus. Error-controlled adaptive goal-oriented modeling and finite element approximations in elasticity. *Computer Methods in Applied Mechanics and Engineering*, 196(37–40):3598 – 3613, 2007. Special Issue Honoring the 80th Birthday of Professor Ivo Babuška.

[20] T. Pannachet, P. Díez, H. Askes, and L.J. Sluys. Error assessment and mesh adaptivity for regularized continuous failure models. *Computer Methods in Applied Mechanics and Engineering*, 199(17–20):961 – 978, 2010.

[21] C. Zaccardi, L. Chamoin, R. Cottereau, and H. Ben Dhia. Error estimation and model adaptation for a stochastic-deterministic coupling method based on the arlequin framework. *International Journal for Numerical Methods in Engineering*, 96 (2):87–109, 2013.

[22] O.A. González-Estrada, E. Nadal, J.J. Ródenas, P. Kerfriden, S.P.A. Bordas, and F.J. Fuenmayor. Mesh adaptivity driven by goal-oriented locally equilibrated superconvergent patch recovery. *Computational Mechanics*, 53(5):957–976, 2014.

[23] J.P. Whiteley and S.J. Tavener. Error estimation and adaptivity for incompressible hyperelasticity. *International Journal for Numerical Methods in Engineering*, 99 (5):313–332, 2014.

[24] R. Rannacher and F.-T. Suttmeier. A feed-back approach to error control in finite element methods: application to linear elasticity. *Computational Mechanics*, 19(5): 434–446, 1997.

[25] R. Rannacher and F.-T. Suttmeier. A posteriori error control in finite element methods via duality techniques: Application to perfect plasticity. *Computational Mechanics*, 21(2):123–133, 1998.

[26] R. Rannacher and F.-T. Suttmeier. A posteriori error estimation and mesh adaptation for finite element models in elasto-plasticity. *Computer Methods in Applied Mechanics and Engineering*, 176(1–4):333 – 361, 1999.

[27] F.-T. Suttmeier. On plasticity with hardening: Adaptive finite element discretization. *Int. Math. Forum*, 52:2591 – 2601, 2010.

[28] D. W. Kelly, J. P. De S. R. Gago, O. C. Zienkiewicz, and I. Babuška. A posteriori error analysis and adaptive processes in the finite element method: Part i — error analysis. *International Journal for Numerical Methods in Engineering*, 19(11):1593–1619, 1983.

[29] S.Sh. Ghorashi, T. Lahmer, A.S. Bagherzadeh, and T. Rabczuk. Goal-oriented error estimation and mesh adaptivity in elasticity problems with heterogeneous material distribution. *Engineering Geology*, submitted.

[30] S.Sh. Ghorashi, J. Amani, A.S. Bagherzadeh, and T. Rabczuk. Goal-oriented error estimation and mesh adaptivity in three-dimensional elasticity problems. *WCCM XI- ECCM V - ECFD VI, Barcelona, Spain*, 2014.

[31] S.Sh. Ghorashi and T. Rabczuk. Goal-oriented error estimation and mesh adaptivity in 3d elastoplasticity problems. *International Journal of Fracture*, pages 1–17, 2016. ISSN 1573-2673.

[32] W. Bangerth, R. Hartmann, and G. Kanschat. Deal.ii—a general-purpose object-oriented finite element library. *ACM Transactions on Mathematical Software*, 33 (4), August 2007.

[33] W. Bangerth, T. Heister, L. Heltai, G. Kanschat, M. Kronbichler, M. Maier, B. Turcksin, and T. D. Young. The `deal.II` library, version 8.2. *Archive of Numerical Software*, 3, 2015.

[34] C. Chen and O.L. Mangasarian. Smoothing methods for convex inequalities and linear complementarity problems. *Mathematical Programming*, 71(1):51–69, 1995.

[35] P. Areias and T. Rabczuk. Smooth finite strain plasticity with non-local pressure support. *International Journal for Numerical Methods in Engineering*, 81(1):106–134, 2010.

[36] P. Areias and T. Rabczuk. Finite strain fracture of plates and shells with configurational forces and edge rotations. *International Journal for Numerical Methods in Engineering*, 94(12):1099–1122, 2013.

[37] J. Frohne, T. Heister, and W. Bangerth. Efficient numerical methods for the large-scale, parallel solution of elastoplastic contact problems. 105(6):416–439, 2015.

[38] J.C. Simo and T.J.R. Hughes. *Computational inelasticity*. Springer, 1998.

[39] M. Sauter and C. Wieners. On the superlinear convergence in computational elasto-plasticity. *Computer Methods in Applied Mechanics and Engineering*, 200(49–52): 3646–3658, 2011.

[40] J. Nocedal and S.J. Wright. *Numerical Optimization*. Springer Series in Operations Research, Springer, New York, 1999.

[41] K.J. Bathe. *Finite element procedures*. Prentice Hall, Englewood Cliffs, NJ, 1996.

[42] M. Ainsworth and J.T. Oden. A posteriori error estimation in finite element analysis. *Computer Methods in Applied Mechanics and Engineering*, 142(1–2):1 – 88, 1997.

[43] T. Grätsch and K.J. Bathe. A posteriori error estimation techniques in practical finite element analysis. *Computers & Structures*, 83:235–265, 2005.

[44] P. Ladevéze and L. Chamoin. Calculation of strict error bounds for finite element approximations of non-linear pointwise quantities of interest. *International Journal for Numerical Methods in Engineering*, 84(13):1638–1664, 2010.

[45] X.-L. Gao. Elasto-plastic analysis of an internally pressurized thick-walled cylinder using a strain gradient plasticity theory. *International Journal of Solids and Structures*, 40(23):6445 – 6455, 2003.

[46] P.S. Theocaris and E. Marketos. Elastic-plastic analysis of perforated thin strips of a strain-hardening material. *Journal of the Mechanics and Physics of Solids*, 12 (6):377 – 380, 1964.

[47] W.K. Liu, T. Belytschko, and A. Mani. Random field finite elements. *International Journal for Numerical Methods in Engineering*, 23(10):1831–1845, 1986.

[48] P. Constantine. Random field simulation. file exchange @ matlab central, 2010.

[49] Michael W. Davis. Production of conditional simulations via the lu triangular decomposition of the covariance matrix. *Mathematical Geology*, 19(2):91–98, 1987.